



Università
degli Studi
della Campania
Luigi Vanvitelli

Dipartimento di Matematica e Fisica

**Investigation on the applicability of
immunodetection techniques to biomolecule
samples concentrated via
pyro-electrohydrodynamic jet**

DOCTOR OF PHILOSOPHY THESIS

Supervisor: *Dr. Simonetta Grilli*

Candidate: *Danila del Giudice*

Summary

List of publications and proceedings.....	7
The scenario of the PhD thesis.....	8
Chapter 1 general introduction.....	11
1.1 Alzheimer's Disease.....	11
1.1.1 Current therapies	14
1.1.2 AD diagnosis: current approach and their limits.....	15
1.2 Biosensors	16
1.3 Pyro-Electrohydrodynamic Jet	17
1.3.1 Electrohydrodynamic effect.....	18
1.3.2 Pyro-electrohydrodynamic jet.....	19
1.3.2.1 P-jet applications.....	20
Chapter 2 Preliminary experiment tests	22
2.1 Material tested in other to optimize the protocol	23
2.1.1 Choice of the reaction support.....	23
2.1.2 Buffer solutions to stabilize the sample droplets.....	24
2.1.3 Reagents for the reaction support	24
Test 1.....	25
Test 2.....	26
Test 3.....	27
Test 4.....	29
Test 5.....	29
Chapter 3 Materials and methods	32
3.1 Lithium niobate and the pyroelectric effect.....	32
3.2 Slides	32
3.3 A β 1-42 protein solution for immunoreaction.....	32
3.4 A β 1-42 protein solution for rheological characterization	33
3.5 Fluorescent probes.....	33
3.6 Immunoreaction protocol	33
3.7 Spot's signal: acquisition and analysis.....	33
3.8 The piezo-driven biospotter	34
3.9 The pendant drop tensiometer	35
3.10 Sample interfacial tension measurements.....	37
3.10.1 Preliminary tests and definition of the measurement protocol.....	37

3.10.2 Mathematical models	39
3.11 Determination of the fluorescence intensity	40
3.12 Statistical Analysis	40
Chapter 4 Results and discussions	41
4.1 Reproducibility of the p-jet spots.....	41
4.2 Characteristic curves of the p-jet accumulation	42
4.3 Comparison with S3 biospotter dispensed samples.....	44
4.4 Application for immunodetection of A β 1-42	46
4.5 Surface tension measurements.....	47
4.6 Fluorescence intensity measurements	51
Chapter 5 Conclusions.....	53
References	56

List of publications and proceedings

Mugnano, M., Lama, G. C., Castaldo, R., Marchesano, V., Merola, F., Del Giudice, D., ... & Grilli, S. (2019). **Cellular uptake of mildly oxidized nanographene for drug-delivery applications.** *ACS Applied Nano Materials*, 3(1), 428-439.

Rega, R., Mugnano, M., Oleandro, E., Tkachenko, V., Del Giudice, D., Bagnato, G., ... & Gangemi, S. (2020). **Detecting collagen molecules at picogram level through electric field-induced accumulation.** *Sensors*, 20(12), 3567.

Rega, R., Mugnano, M., Del Giudice, D., Itri, S., Tkachenko, V., Vespini, V., ... & Grilli, S. (2020, April). **Highly sensitive detection of low abundant molecules by pyro-electrohydro-dynamic jetting.** In *Biophotonics in Point-of-Care* (Vol. 11361, pp. 41-51). SPIE.

Miccio, L., Pirone, D., Sirico, D., Merola, F., Memmolo, P., Bianco, V., ... & Ferraro, P. (2022, May). **Tomographic phase microscopy at single cell scale without a-priori knowledge of cell orientations: smart strategies for rotation angles recovery.** In *Unconventional Optical Imaging III* (Vol. 12136, pp. 211-217). SPIE.

Mugnano, M., Lama, G. C., Castaldo, R., Merola, F., del Giudice, D., Grilli, S., ... & Ferraro, P. (2021, June). **Cytocompatibility and 3D biodistribution with oxidized nanographene assessed by digital holographic microscopy.** In *Optical Methods for Inspection, Characterization, and Imaging of Biomaterials V* (Vol. 11786, pp. 72-77). SPIE.

Tkachenko, V., Schwödiauer, R., Rega, R., Itri, S., Mugnano, M., del Giudice, D., ... & Grilli, S. (2022). **High-Rate Accumulation of Tiny Aqueous Droplets Using a Pyroelectrohydrodynamic Jet System.** *Advanced Engineering Materials*, 24(3), 2100756.

Pirone, D., Sirico, D., Miccio, L., Bianco, V., Mugnano, M., del Giudice, D., ... & Ferraro, P. (2021). **Lipid droplets 3D full measurement by holographic in-flow tomography.** *bioRxiv*.

Itri, S., del Giudice, D., Mugnano, M., Tkachenko, V., Uusitalo, S., Kokkonen, A., ... & Grilli, S. **A Pin-Based Pyro-Electrohydrodynamic Jet Sensor for Tuning the Accumulation of Biomolecules Down to Sub-Picogram Level Detection.** Available at SSRN 4142162.

Rega, R., Mugnano, M., Del Giudice, D., Itri, S., Tkachenko, V., Vespini, V., ... & Grilli, S. (2021, June). **SensApp: a FET-open project for developing a supersensor able to detect Alzheimer's disease biomarkers in blood.** In *Optical Methods for Inspection, Characterization, and Imaging of Biomaterials V* (Vol. 11786, p. 1178605). SPIE.

Běhal, Jaromír, et al. **On monocytes and lymphocytes biolens clustering by in flow holographic microscopy.** *Cytometry Part A*.

Danila del Giudice et al. **Innovative biosensor for testing the astronaut health during spaceflight** 2022 IEEE 9th

Sara Coppola et al. **Polymeric microneedles: design of a biomedical patch** 2022 IEEE International Workshop on Metrology for Industry 4.0 & IoT (MetroInd4.0&IoT)

The scenario of the PhD thesis

The huge increase of dementia cases has led the European Government to undertake several actions in support of the patients, funding a series of projects to find innovative methods for early diagnosis and possible treatments. Among the forms of dementia stands out Alzheimer's disease (AD). The aim of the institutions is to ensure dignity and autonomy for people that live with dementia, to improve their lives, change society's perceptions, and dismiss this stigma. My thesis work was integrated into this scenario, indeed it was part of the European SensApp project "Super-sensitive detection of Alzheimer's disease biomarkers in plasma by an innovative droplet split-and stack approach" (SensApp), a FET-open project funded by the Horizon 2020, the funding program of the European Commission. This project was the sum of shared efforts by a consortium of 6 European partners, which include Consiglio Nazionale delle Ricerche - Istituto di Scienze Applicate e Sistemi Intelligenti (CNR-ISASI) and IRCCS Centro Neurolesi "Bonino Pulejo", both from Italy; Vrije University of Brussels (VUB) from Belgium; University of Linz (JKU) from Austria; Technical Research Centre of Finland (VTT) and Ginolis OY (GIN) from Finland.

The project aim was to develop an innovative biosensor with a high sensitivity, to detect low abundant protein biomarkers in small volumes of blood (<1mL), pushing the sensitivity well below 1 pg/mL, thus overcoming the current standard limits. Current clinical diagnostic criteria for AD require a patient to have clear symptoms of dementia which are excluded from other brain disorders, such as memory loss and confusion, inability to learn new things, difficulty with language and so on. Currently, the main bodily fluid used in the detection of AD biomarkers is the cerebrospinal fluid (CSF). The biomarkers total tau, phosphorylated tau (p-tau181 and p-tau231) and β -amyloid1-42 have high diagnostic accuracy in it. The CSF is in direct contact with the extracellular space of the brain and can reflect biochemical changes that occur in pathological progress. Therefore, it is the optimal source of AD biomarkers, but its limit is related to the invasiveness of sample collection. In fact, collecting the cerebrospinal fluid is necessary to make the lumbar puncture procedure, with hospitalization of the patient, already mentally fragile. For all these reasons the use of blood as a sample could overcome these difficulties, having a friendlier withdrawal. On the other hand, the current limit of the use of this fluid is due to the extremely low concentration (50-100 pg/mL) of the AD biomarkers in peripheral blood. Numerous non-core approaches have been proposed in the scientific literature to improve this sensitivity, such as Surface Plasmon Resonance (SPR); biological barcode analysis; Plasmonic ELISA; Digital ELISA; MALDI-TOF mass spectrometry¹. Although they showed a noticeable improvement in sensitivity, they all have limited success in routine clinical practice, in the example, their common denominator was the use of highly expensive technologies, often based on laser ionization, thin coatings, magnetic or specific nanoparticles, or nano-well

platforms, accessible only to highly specialized laboratories. Moreover, they all require time-consuming and crucial sample preparation that moves away from routine practice, thus adding errors to the assay and the need for highly qualified personnel. On the other hand, these procedures required sample volumes of at least tens of μL , thus limiting applications with very small volumes. All of these criticisms hinder mass production and accessibility to routine clinical trials.

In this framework the project SensApp aims at developing an innovative technology called “droplet split and stack” (DSS), able to accumulate low abundant biomolecules and thus pushing the limit of detection down to sub-picogram levels. The DSS makes use of a novel technique based on pyro-electro-hydrodynamic (p-jet) dispensing. The implementation of a high sensitive biosensor based on the DSS technology will open the route to a non-invasive early diagnosis through peripheral body fluids and, as a consequence, to a highly efficient screening programs among patients. The envisaged super-sensor could also offer an easy clinical instrument for rapid and efficient early diagnosis of different serious diseases, often difficult to diagnose for the obsolete method used, through a simple blood test to be engaged in routine practice, useful for population screening programs as well as for follow-up programs during therapies. The first tests were performed for AD biomarkers but the research activity will continue in case of other severe diseases that require the quantification of low abundant analytes in bodily fluids.

In general, this approach was able to accumulate low abundant biomolecules, of various types, by depositing tiny droplets of the target solution onto a micrometre-scale binding site of a functionalized glass slide. This allowed the antigen-antibody reaction to occur in sub-microliter volumes, avoiding the diffusion phenomena usually occurring in standard procedures, and significant improving of the fluorescence (FL) signal per unit area, reducing the limit of detection (LOD). After the biomarkers' deposition with this approach, to quantify the biomolecules, the analytes were involved in an immunoassay with a secondary antibody labelled with a fluorophore, this allowed for detecting the molecules and quantifying the signal intensity (Fig. 1).

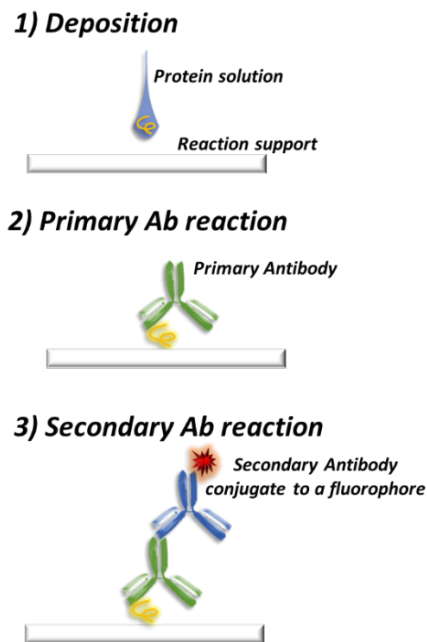


Figure 1. Schematic view of the immunoassay steps to detect biomolecules.

The immunoassay took advantage of affinity binding between antibodies and the corresponding antigens that allowed the detection of one of these, even if it was present at very low concentrations and in complex biological matrices such as whole blood, serum, and other biological fluids. The antigen-antibodies binding was specific, and the recognition of the antibodies with the biomarkers was conformation-dependent, indeed protein aggregation could have limited this phenomenon. Moreover, the AD biomarkers aggregation and precipitation are the features that led to the toxicity.

My thesis work was focused on the development of an immunoassay protocol for detecting the AD biomarkers compatible with the DSS technology implemented during the SensApp project mentioned above. Considering the impact of the aggregation biomarkers on the immunoreaction protocol and in general on the toxicity of the protein involved in the AD, my work included the definition of a non-destructive and simple method to investigate the effects of protein agglomeration on the immunoreaction protocol and rheological properties of the samples under test. It was evaluated the variation of the interfacial tension (IFT) of the Amyloid β 1-42 for 30 days. The synthetic biomarkers were tested for immunoassay in parallel with the IFT measurement, to correlate the variation of the protein structure with the loss of the antigen-antibody bond specificity

Chapter 1 general introduction

1.1 Alzheimer's Disease

There are more and more new cases of dementia every year, AD emerges as the most common form of late-life mental failure in humans. It is well known that AD is a serious disease currently very widespread in the world population. The World Health Organization Report reports alarming growth estimates of dementia: 35.6 million cases in 2010 that will double in 2030 and triple in 2050 with 7.7 million new cases per year². The major risk factors include genetic correlation with *apolipoprotein E4* and family history, traumatic brain injury, hypercholesterolemia, obesity, hypertension, diabetes, and low education level³. AD is a complex progressive condition with neuropathological cascades that interact sequentially. This pathological condition was unclear until the 1960s when electron microscopy helped Michael Kidd in England and Robert Terry in the United States to understand the two classical lesions: senile or neuritic plaques and neurofibrillary tangles⁴. These produce several pathogenic mechanisms as well as neurovascular dysfunctions, inflammatory processes, oxidative stress, and mitochondrial dysfunctions, until to degeneration of neurons and synapses⁵; these damages lead to an irreversible loss of brain tissue⁶. In figure 2 it is possible to appreciate the significative differences between the healthy control versus a pathological magnetic resonance imaging.

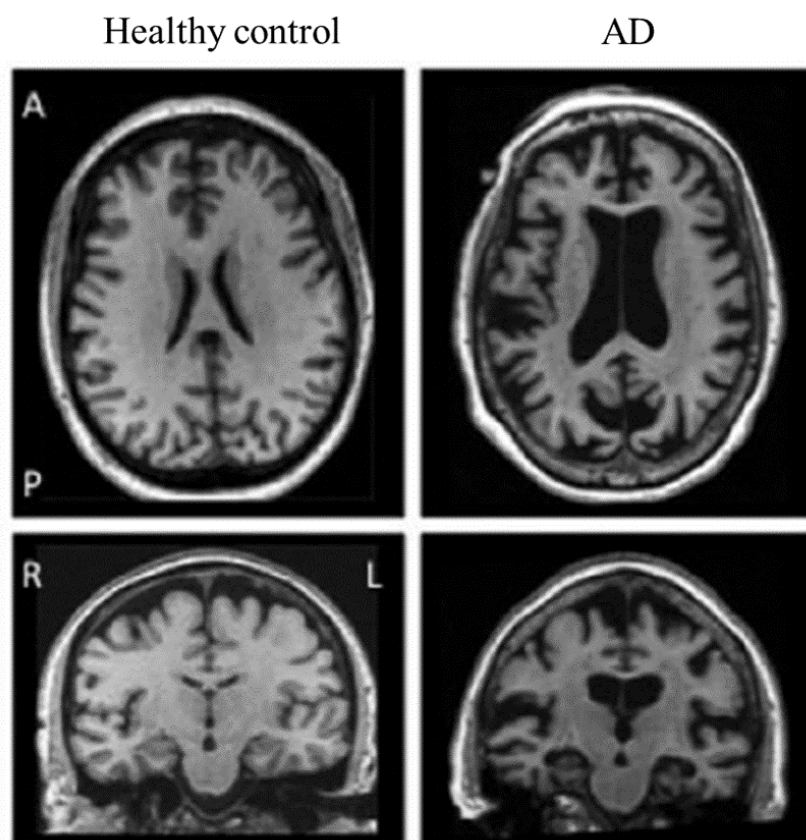


Figure2. Typical Alzheimer's disease brain atrophy compared to healthy control in magnetic resonance imaging. L = left. R = right. A = anterior. P = posterior.

A serious loss of the hippocampal volume is found in the AD subjects compared with the controls⁷. The typical AD group is included in the abnormal medial temporal atrophy (MTA) in conjunction with either an abnormal posterior atrophy (PA) or global cortical atrophy-frontal (GCA-F), or an abnormal MTA in conjunction with both an abnormal PA and GCA-F⁶. Moreover, the clinical manifestations of AD are not only associated with regional grey matter deterioration, but also with pathological integration between cortical brain regions⁸. As already mentioned, among the major features of this distressing disease are the growth of the neuritic of β -amyloid peptides. Fibrillar Amyloid β protein ($A\beta$) can activate microglia, leading to the production of toxic and inflammatory mediators like hydrogen peroxide, nitric oxide, and cytokines. The neuritic plaques are microscopic extracellular amyloid deposition in the brain, associated with axonal and dendritic injury, often found in large numbers in the limbic and association cortices. These are composed of aggregates of $A\beta$ ⁹. The time employed to develop the plaque is unknown, but these lesions probably evolve very gradually over months or years. Their diameter in microscopic brain sections has a wide variety. The exact mechanism of Amyloid β protein formation in AD is not well clear. Based on data accumulated so far, the plaques are composed of Amyloid β ending predominantly with amino acid 42 ($A\beta$ 1-42) and, a smaller amount, with amino acid 40 ($A\beta$ 1-40). Both are enzymatically released from the Amyloid Precursor Protein (APP)¹⁰. Recent studies highlight the importance of the $A\beta$ 1-40/1-42 ratio, an important factor for AD progression and disease severity¹¹. Human APP belongs to a highly conserved family of type 1 transmembrane glycoproteins (Fig.3A). APP influences neurogenesis with its domains: the soluble secreted APPs and the APP intracellular domain. The first protects neuron cells and promotes neurogenesis, whereas the second modulates neurogenesis negatively¹². The balance of APP metabolism is fundamental, interruption of this disrupts downstream balances and finally contributes to AD. APP can undergo amyloidogenic or non-amyloidogenic processing via cleavage by different secretases. In fact, the Amyloid-beta peptides derived by APP through sequential proteolytic processing of β and γ secretases: APP is first processed by the β -secretase obtaining sAPP β . The last 99 amino acids of the APP C-terminus remain in the membrane. Subsequently, it is cleaved by γ secretases in 38–43 amino acids from the N-terminus leading to the generation of $A\beta$ peptides, a third fragment after γ -secretase cleavage is released into the cytoplasm (Fig.3B)¹³.

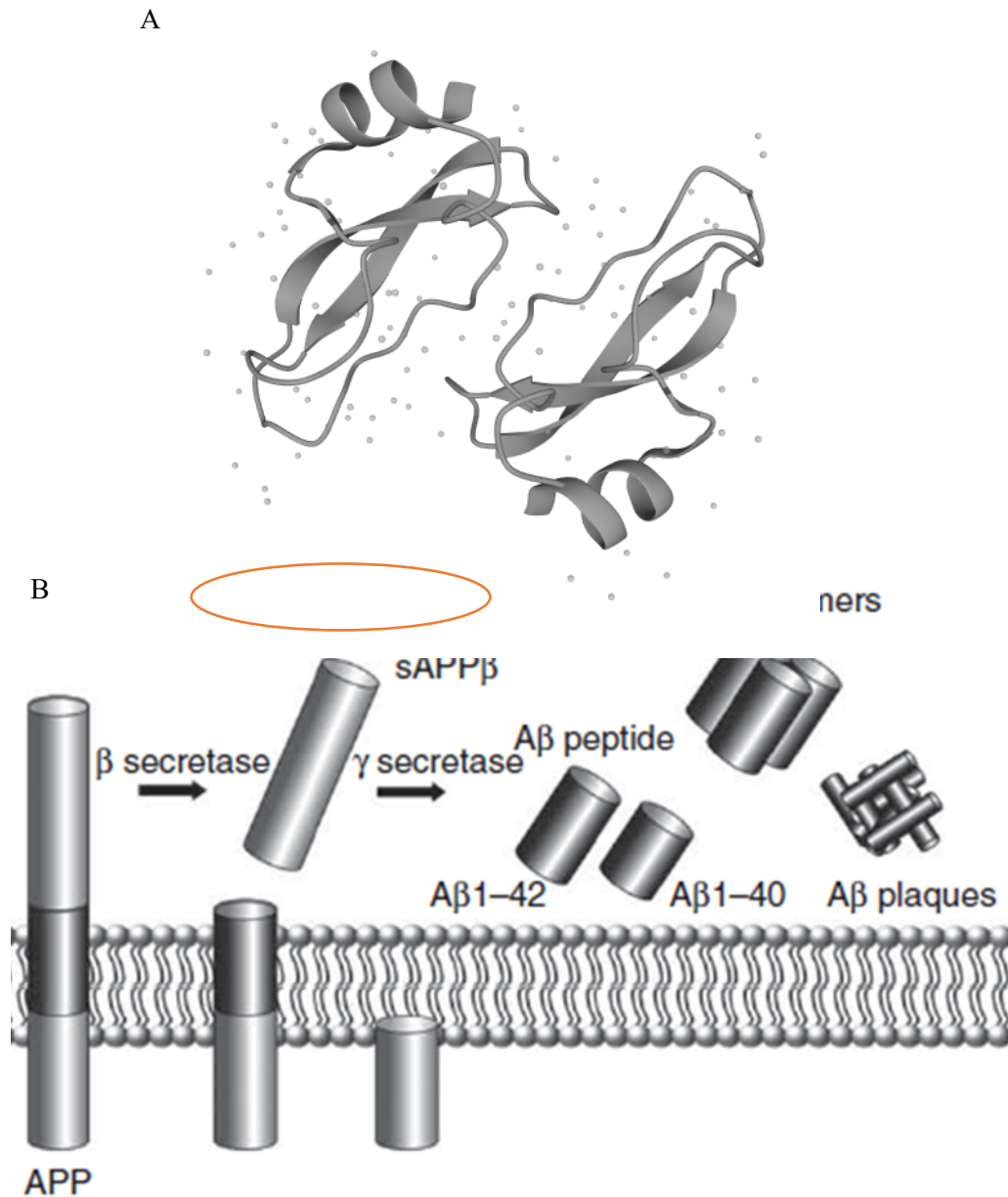


Figure3. A) APP 3D structure¹⁴; B) APP processing thanks to β and γ secretases, which leads to A β plaques.

The mutations in APP are responsible only for a small proportion of AD cases. Indeed, most cases seem to suggest that there must be other causes of the disease, still not fully understood. Interesting studies have identified possible cause also in mutation on the presenilin protein, which enhances the processing of APP to form amyloidogenic A β ¹⁵. The toxicity of the amyloid peptides is dependent upon their propensity to aggregation state^{16,17}. Proteins can aggregate in the native state, through the formation of chemical bonds or self-assembling, or as unfolded intermediate conformations when are mutated, intervening a series of complex factors that lead to the fibrillar aggregates, the amyloid fibrils¹⁸. Indeed, non-native proteins lost functions and are particularly prone to aggregation. Through computational study on the competition between folding and aggregation of proteins, V. Bianco et

all demonstrated a correlation between concentration, the complete loss of the folded structures and the formation of protein aggregates(**Figure 4**)¹⁹.

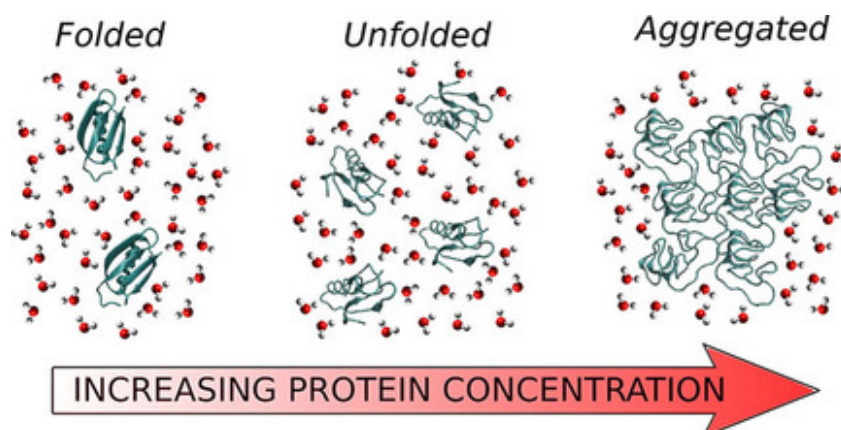


Figure 4. Correlation explained in the Bianco et al study¹⁹.

It is not deeply understanding all the aggregation mechanism, reported data indicate that the possible critical step in protein aggregation is the unfolding of the proteins. Unfold protein are more subject to aggregation^{20–22}. This change of configuration characterizes the aggregation and put the protein at risk to become cause of disease such as AD²³.

AD is a slowly progressive disorder, with insidious onset and progressive impairment of the brain functions. AD pathology can have mild or severe cognitive features related also with the early-onset or late-onset. Early-onset is defined when the patients are younger than 65 years of age²⁴. Many differences exist between early-onset and late-onset, even in the causes. Early-onset AD has a significant genetic predisposition involving a direct autosomal dominant transmission and a higher polygenic susceptibility²⁵. Furthermore, many studies analyse the psychological impact of the risk of the genetic predisposition and relative diagnosis of the AD²⁶; in these cases, the genetic test can lead to significant anxiety, and depression, especially when psychological stability is not adequate to receive positive or inconclusive results²⁶. In addition, the early-onset patients have also a potentially more aggressive clinical course and greater risk for mortality^{27,28}. However, regardless of the onset, this disease involves and overwhelms the daily life of the patients. The common symptoms include loss of memory, attention, language, reduced perceptual speed, and executive functioning, their loss of independence causes a heavy personal toll on the patient and the family²⁹. In addition, neuropsychiatric symptoms such as apathy, depression, aggression, agitation, sleep disruption, and psychosis are now recognized as core symptoms of AD that are expressed during the illness course^{30,31}.

1.1.1 Current therapies

Despite the number of patients afflicted by AD is growing, there are currently only five approved treatments to mitigate symptoms, temporarily ameliorating memory and thinking problems. All the

therapy are only symptomatic therapies, they do not treat the underlying cause of AD and do not slow the rate of decline, no one approved drugs is able to prevent, delay, or halt the progression of disease. Current treatments can only delay the onset of AD by approximately 2 years³². AD is a multifactorial disorder, for this reason often the therapies are combined to be more effective than single-agent therapy³³. The combination of more drugs targeting different mechanisms and providing synergistic effects has shown better results. Cholinesterase inhibitors (ChEIs) such as donepezil, galantamine, and rivastigmine are selected for the early stage, while Memantine, an N-methyl-d-aspartate receptor antagonist, and combination of a ChEI and memantine are indicated for moderate-to-severe stages³⁴. In phase III trials most tested drugs failed because they do not reach the target efficacy, even though there are promising results in the initial studies phase. The complex nature of AD is considered as one of the main reasons for the high failure. For the pressure and severity of this pathology, global leaders have set a deadline of 2025 for finding an effective way to treat or prevent AD³⁵.

1.1.2 AD diagnosis: current approach and main limits

The accurate and early diagnosis of AD plays a crucial role in the pathologic evolution. The awareness of the severity and the progression risks provides for taking preventative measures before irreversible brain damages are shaped. A wide range of symptoms appears worst when AD has a late diagnosis²⁹. It has been understood that the typical biomarkers, as well as Amyloid β , become positive decades before the first symptoms manifest. Therefore, well-validated biomarkers have to be processed as soon as possible to improve the design of clinical trials and, in this way, develop more effective therapeutics³⁶. Currently, the unequivocal diagnosis is possible only during a post-mortem biopsy. The most popular techniques used for detecting local brain loss of tissue are nuclear Medicine imaging devices: Positron Emission Tomography (PET) and Single Photon Emission Computed Tomography (SPECT), and Magnetic Resonance Imaging (MRI) to assess major structural changes³⁷. To aid the diagnosis of this serious disease, every field introduce important innovation and support, improving the current methods. An innovative enhancement is submit by Siqui Liu et al, which introduced an improvement based on features extracted from neuroimaging biomarkers, they proposed machine learning methods that conduct AD diagnosis as a multi-class classification task, with minimal knowledge dependency of the patient stage³⁸.

Nowadays the clinical practice is based on the biomarkers quantification in Cerebrospinal fluid (CSF). They use a small amount of CSF because of the higher amounts of biomarkers present. Unfortunately, CSF collection requires a highly invasive and risky intervention of lumbar puncture on the patient, considering also additional health complications in an already precarious clinical situation. This procedure is not easily applicable for follow-up of the disease progression during therapy, moreover this procedure requires hospitalization of the sick person. The use of bodily fluids such as plasma would make diagnosis more accessible with an easier population screening. The use

of plasma fluid is not yet used because in this complex matrix, the reproducibility and accuracy in the measurements of Amyloid is a challenging task, it is also due to the unstable nature of the peptide and the biochemical heterogeneity of the A β fragments. Until now, with this approach the available assay formats and technologies yield insufficient analytic sensitivity. For experimental early disease diagnosis, through biomarkers determination in peripheral body fluids, it can be adopted immunoassays based on kits for Enzyme-Linked Immuno Sorbent Assay (ELISA), chemiluminescence³⁹ or electrochemiluminescence⁴⁰. In general, the ELISA kits are the gold standard of the immunoassay, they are in the market like platforms for diagnostic purposes, such as Fujirebio. This approach, even though is easy and common in the clinical field, in this case limit the sensibility, in example, the Fujirebio kit, just mentioned, has a LOD of 62.6 pg/mL⁴¹, too high to be capable of a real early diagnosis compared to the development of symptoms.

New technologies about proteomics are developing new methods of mass spectrometry-based able to identify and quantify proteins from biological samples⁴². However, these approaches require a huge economic, tools, and skills effort, so nowadays it is impossible to transfer these skills to routine clinical practice. In a heterogenous solution, the biomarker detection is heavily dependent on the correct protein folding and hence the affinity for specific antibodies, which react with particular sequences of the analytes^{43,44}. Nevertheless, in the antibody reaction plays a crucial role the aggregation status of the protein. If the proteins are misfolding, the antibodies cannot recognize the epitopes, the site-specific antibody conjugation. This limits the detection of the biomolecules, reducing the intensity of the signal, developing a false negative result.

1.2 Biosensors

One of the most challenges of the last decades is the rapid detection of some important analytes involved in the pathophysiological processes. Nowadays, many assays are proposed to measure different kinds of biomarkers: matrix-assisted laser desorption ionization–time of flight (MALDI–TOF) mass spectrometry, used for protein quantification¹, antigen capture ELISA to detect virus⁴⁵, ultrasensitive Simoa technology, that offers important improved analytical sensitivity⁴⁶. In this scenario, the biosensor approach emerges as one of the most promising platforms for this purpose.

A biosensor is composed of two main correlated elements:

- an immobilized *bioreceptor*, that can recognize the analyte of interest, which can be antibodies, oligonucleotides, or enzymes, the latter is the most commonly used biosensing element in biosensors;
- a *transducer*, that is used to convert the interaction of the analytes with the bioreceptor in the (bio)chemical or electronic signal. The intensity of the signal is directly or inversely proportional to the biomarker concentration^{47–49}.

The biosensors are devices that are able to estimate the level of various biomarkers like proteins but also RNA, DNA, or pathogens⁵⁰; according to their use, they can be of various types such as enzyme-

based, tissue-based, immunosensors, DNA biosensors^{51–55}. The first enzyme-based immunosensor is reported in 1967, these biosensors are based on the immobilization of an enzyme which recognizes the analytes. Various immobilization strategies can be envisioned: adsorption, covalence, entrapment, cross-linking or affinity^{48,56}. Nucleic acids have acquired a relevant role in a wide range of biosensors and bioanalytical assays. With these biosensors, the sensing elements are oligonucleotides, with a known sequence of DNA or RNA^{57,58}. While the immunosensors have immobilized immunological receptors, the antibodies, bind the target analytes, taking advantage of the structural complementarity⁵⁴. Indeed, this approach exploits the extremely specific antibody-antigen binding, which provides sensitive ways to detect molecules such as bacteria, viruses, proteins and so on⁵⁹. Existing biosensors are limited when the abundant biomarker concentration in biological samples is under 10 pg/mL. Additionally, the LOD of the standard techniques often makes useless the intense researcher efforts and prevents the use of the biosensors to perform their studies. In this scenario, with their flexibility, the biosensors can potentially fulfil the necessity of analytical performance for a wide range of applications in many fields namely the food industry, medical field, marine sector etc.

1.3 Pyro-Electrohydrodynamic Jet

The research activity in this thesis is focused on the development of a reliable technique for immobilizing and detecting the target proteins in low abundant samples, dispensed through the innovative Pyro-Electrohydrodynamic Jet (p-jet) for highly sensitive detection able to overcome the current LOD encountered in conventional ELISA-based assays. Pyroelectricity is defined as the temperature dependence of the spontaneous polarization (P_s) in certain anisotropic solids. Some crystals have the property to generate this spontaneous change of polarization, when they are heated developing a temporary electric field, this effect is the so-called *pyroelectric effect*⁶⁰. The unit cells of pyroelectric materials have a dipole moment, when the temperature is constant each dipole has its orientation, and the total electric dipole moment is zero. The temperature increase produces a redistribution of charges to compensate for the change and so it is obtained a dipole moment with a charge displacement on the material surface, resulting in a current flow.

Figure5 A shows the schematic side view of the pyroelectric crystal at equilibrium, when the spontaneous polarization P_s is completely shielded by the external screening charge, while Fig.5B shows the condition occurring when the crystal is stimulated through a temperature variation. In this case the magnitude of P_s varies generating a transient surface charge density $\alpha = p_i \Delta T$ due to the uncompensated charges. A high electric field (ENL 10^7 V/m) is generated on the surface of the crystal. As explained in previous works^{61–63}, the spontaneous polarization P_s changes according to $\Delta P_i \propto p_i \Delta T$, where P_i is the coefficient of the polarization vector, p_i is the pyroelectric coefficient and ΔT is the temperature variation ($p_i = -8.3 \times 10^{-5} \text{ C m}^{-2} \text{ }^\circ\text{C}^{-1}$ for LN at 25 °C).

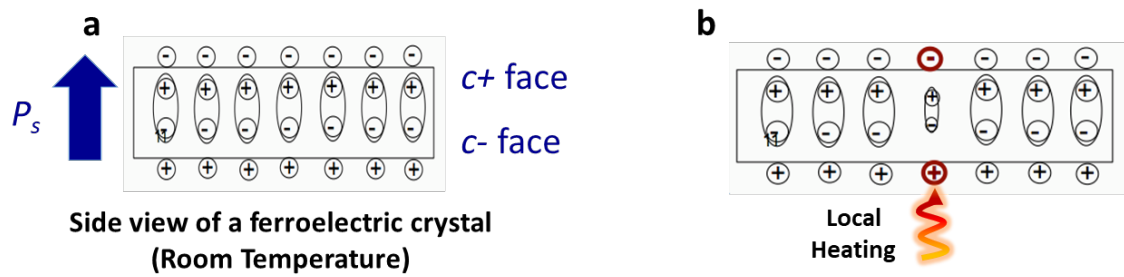


Figure 5. Side view of a ferroelectric crystal: a) at room temperature; b) under a local temperature variation. The red circles indicate the transient uncompensated charges that generate a high electric field.

1.3.1 Electrohydrodynamic effect

The electrohydrodynamic effect is a well-known phenomenon on how the application of an external electric field regulates the liquid motion. [Ref: Advanced Materials Interfaces 8, 2000670 (2021)], for example forming droplets exiting from nozzles or orifices⁶⁴. When the liquid becomes unstable under the stimulation, the end develops in an axial jet. This happens because on the interface there is a charge reorganization that leads the liquid in the direction of the field, in this way the sample generates a typical conical shape: Taylor's cone⁵³ (Fig.6). It is an equilibrium condition between the forces generated by the external force applied and its surface tension force⁶⁶. EHD inkjet head can produce droplets smaller than the size of the nozzle, but it uses external electrodes that are affected by possible cross-contaminations and detrimental clogging of the orifice.

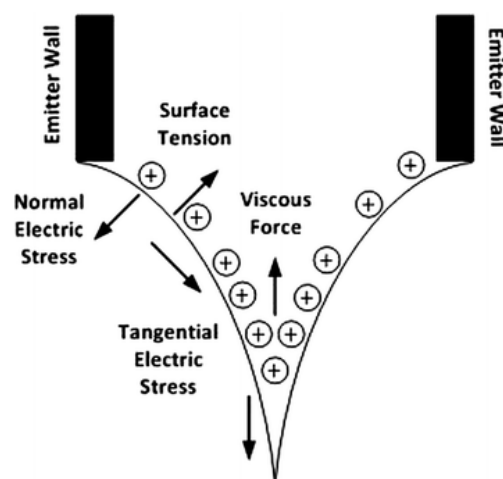


Figure 6. Charge rearrangement after external electric stimulation.

1.3.2 Pyro-electrohydrodynamic jet

The use of external electrodes in EHD can be avoided by employing the intrinsic property of the pyroelectric crystals to develop surface charges when subjected to a thermal gradient. We can call this effect “pyro-electro-hydro-dynamics (pyro-EHD)”⁶⁷, in analogy with the more traditional EHD cited previously. The evolution of the electric field created by a pyroelectric crystal (i.e. Lithium Niobate-LiNbO₃, LN) called a pyro-electrohydrodynamic jet (p-jet) allows one to deposit separate droplets with relatively low volumes^{62,68}. The LN thermally stimulated creates a strong electric field that deforms the liquid meniscus into a conical profile which is maintained until a specific threshold of the electric potential is reached. Tiny droplets are released from the liquid apex when the surface tension of the liquid is overcome (Fig7).

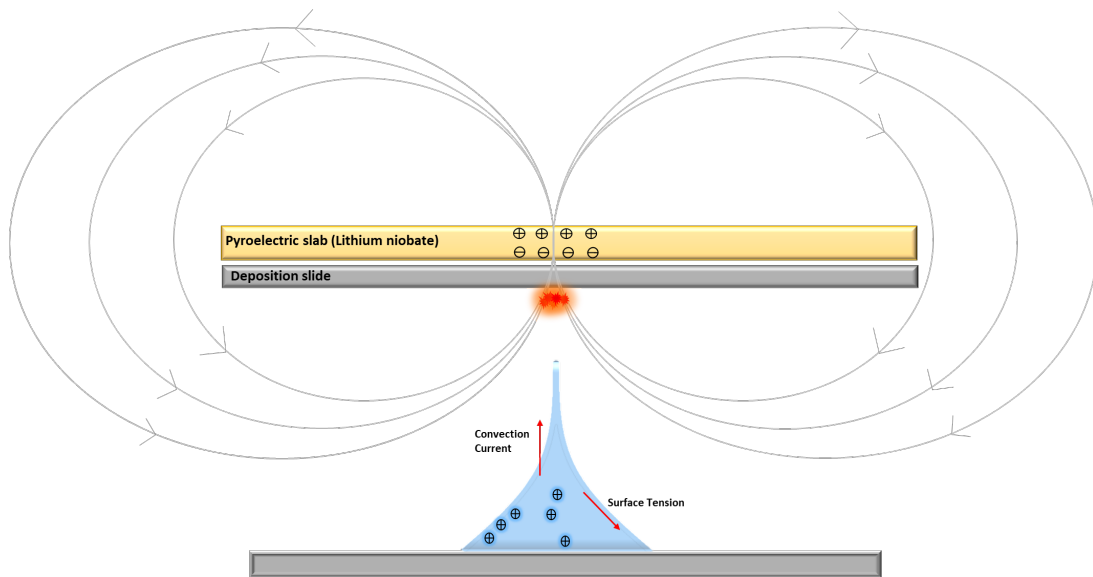


Figure 7. Schematic view of a liquid drop deformation under the action of the electric field generated by a pyroelectric crystal.

The overall experimental p-jet set-up is depicted schematically in Figure 8.

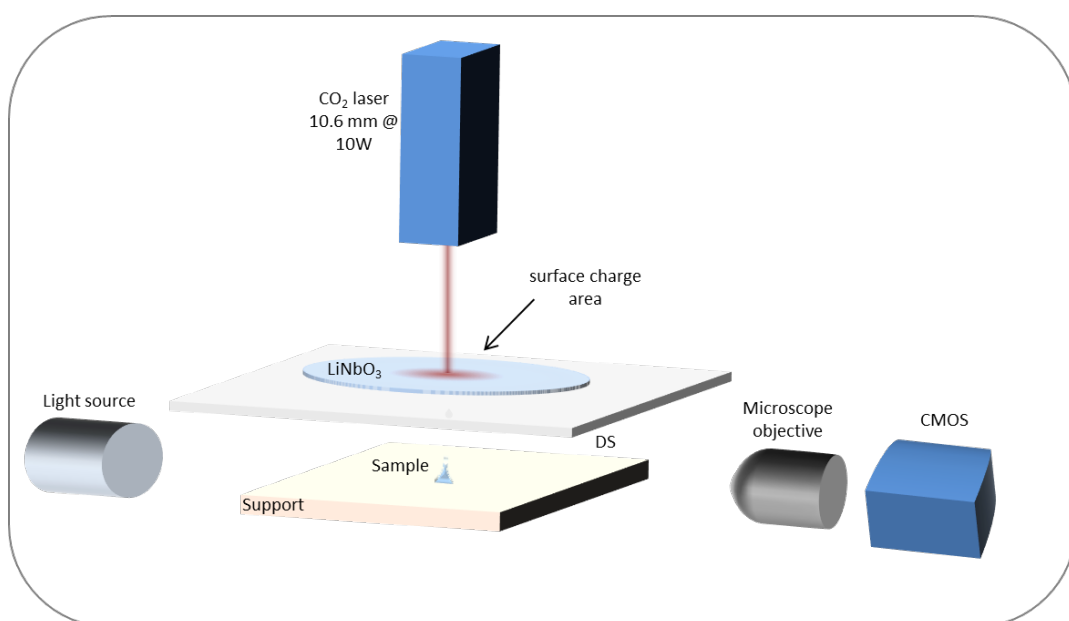


Figure 8. The sample is accommodated on a hydrophobic support. The deposition slide (DS) (used for binding the sample molecules) is mounted onto a conventional tilting clamp. A pyroelectric crystal (z-cut LiNbO₃, 500 μm thick) is mounted onto a separate three-axis translation stage over the DS and drives the EHD-dispensing effect when stimulated by the output beam of a CO₂ laser (wavelength 10.6 μm and output power of 10 W). The CO₂ laser output was modulated by a conventional 5V transistor-transistor logic (TTL) signal. An electric field is generated across the thermal-stimulated region of the pyroelectric crystal, thus inducing the pyro-EHD-dispensing effect as described previously. A high-speed CMOS camera (Motion Pro Y3-S1; 10,000 frames per s; pixel size 10.85 x 10.85 μm) captures the dispensing events. INSERIRE QUI REF: Nature Communications 5, 5314 (2014).

1.3.2.1 P-jet applications

The p-jet approach allows different applications. The deposition of small liquid volumes guides the accumulation of biomolecules directly onto a restricted area of the deposition slide. Thanks to this approach it is possible to obtain an increase in sensitivity since it avoids the diffusion phenomenon that generally occurs in conventional methods, significantly increasing the signal-to-noise ratio in fluorescence-based assays^{61–63}. The key concept of this type of approach is called “split and stack”⁶⁹. The p-jet system can detect low abundant biomolecules such as collagen⁶³. Collagens are the most abundant proteins in mammals⁷⁰. Abnormal collagen modification and/or degradation occur in chronic and other pathological conditions, which can generate potential circulating biomarkers in human fluids, useful for an early diagnosis^{71–73}. The ordinary method to quantify markers in body fluid is the enzyme-linked immunosorbent assay (ELISA)^{74,75}. The current LOD of the Human Pro-Collagen I alpha 1, with ELISA assay is 31.2 pg/mL⁷⁶. Collagen biomarker levels in plasma have been associated with survival rates in patients affected by advanced pancreatic cancer⁷⁷, pulmonary arterial hypertension (PAH)⁷⁸, and glioblastoma, the most common and aggressive primary central nervous system tumour^{79,80}. This work is shown serial dilutions of different concentrations of collagen labelled by Alexa Fluor 647. The concentrations of 500 ng/mL, 300, 60, 30, 15 and 3 pg/mL are deposited on the deposition slide. In this work, two different approaches to heating the

pyroelectric crystal were compared. In both cases, the fluorescent signal is evident, in Figure 9 is reported the calibration curves are obtained.

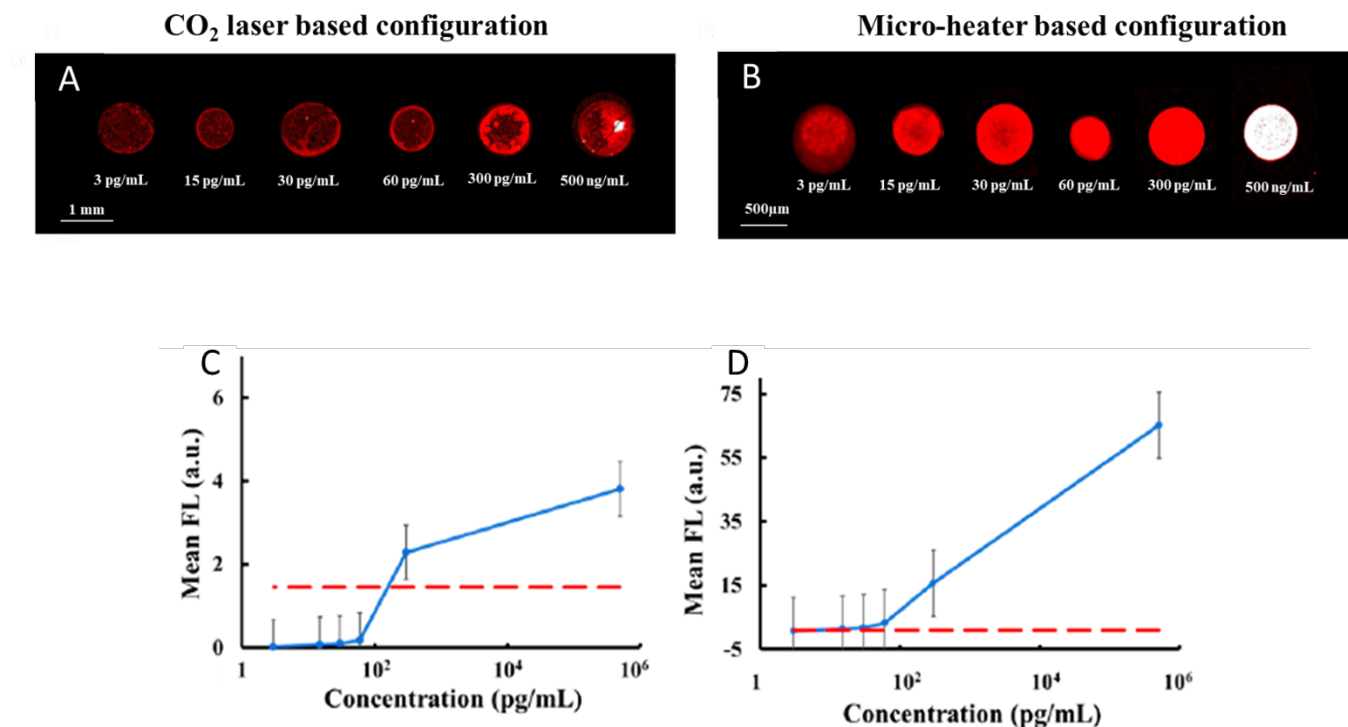


Figure 9. Typical scanner image of the collagen spots: (A) with CO₂ laser configuration; (B) in case of the micro-heater. Plots of mean fluorescence signal as a function of the solution concentration in case of (C) the CO₂ laser and of (D) the micro-heater. INSERIRE QUI REF: Sesnors 20, 3567 (2020).

Chapter 2 Preliminary experimental tests

The first part of thesis work it was implemented an immunoreaction protocol compatible with the droplets deposited by the p-jet on the reaction support. The p-jet approach aims at depositing tiny droplets of sample solution on a micrometric area, to concentrate the fluorescent intensity of the biomarkers obtained after the immunoreaction protocol. It was not straightforward to identify the final reaction protocol. Different aspects were implicated in the process. Figure 10 shows schematically the main protocol steps.

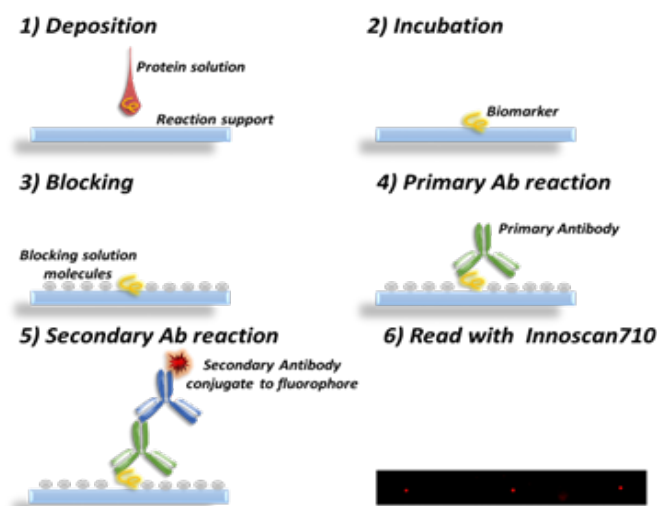


Figure 10. Schematic view of the main protocol steps.

For the first tests a model sample was used, a pure solution of β Amyloid protein fragment 40 dissolved in distilled water. For brevity we call it **Protein solution (PS)** and **protein solution (PS2)** the solution of A β 1-42 dissolved in its appropriate buffer. The PS was chosen for its more stability than the PS2. The A β 1-40, the non-toxic APP product offered a simpler way to involve AD biomarkers, without the instability and the propensity to aggregate the toxic form A β 1-42. Moreover, the A β 1-40 was considered an AD analyte when it was measured in the ratio with the A β 1-42 produced. In this preparatory protocol test, the steps from the blocking solution to the fluorescence reading had fixed conditions, not examined in this preliminary protocol evolution because suggested in the products' datasheets. These fixed steps, called **Antibody Reaction Sequence (ARS)**, were composed by:

- Blocking solution deposition, for saturating non-specific protein-binding sites, improving the assay specificity
- Washing steps, to remove the excess blocking solution
- Primary Antibody reaction, using a specific antibody for the target proteins
- Washing steps to clear away the antibodies that did not bind

- Secondary Antibody reaction, the antibody conjugated with a fluorophore, to label the immune complex
- Washing steps
- Reading step

The following sections illustrate the experimental tests with particular attention on the main issues and variable parameters. The Innoscan 710 (Innopsys) microarray scanner was used for detecting the FL signal emitted by the spots after the reaction of the target molecule with the specific antibodies. We used the MAPIX software associated with the Innoscan 710 for analysing the FL data. For more details about the scanner and the software see the Material section.

2.1 Materials tested for protocol optimization

2.1.1 Choice of the reaction support

Two main types of commercial reaction supports are suggested in literature for immobilizing proteins [Refs]:

1. ONCYTE® Nitrocellulose Film Slides (Grace Bio-Labs, 705278)
2. SuperAmine 2 Ultra Low-Density Microarray Substrate Slides (Arrayit® Corporation, SMM2)

Both were tested in this thesis work. ONCYTE has a 3-dimensional structure composed of porous nitrocellulose, which immobilizes and captures biomolecules thanks to hydrophobic and van der Waals forces. Nitrocellulose films have a long history of use in an immunoassay such as Western, Northern, and dot- (immuno-) blots for reliable immobilization and capture of analytes. They have also been used in the manufacture of lateral flow immunoassays, in the diagnostic industry. The 3dimensional structure of it, supplied a considerably higher surface area for biomarkers binding than the conventional 2-dimensional surfaces (Fig.11).

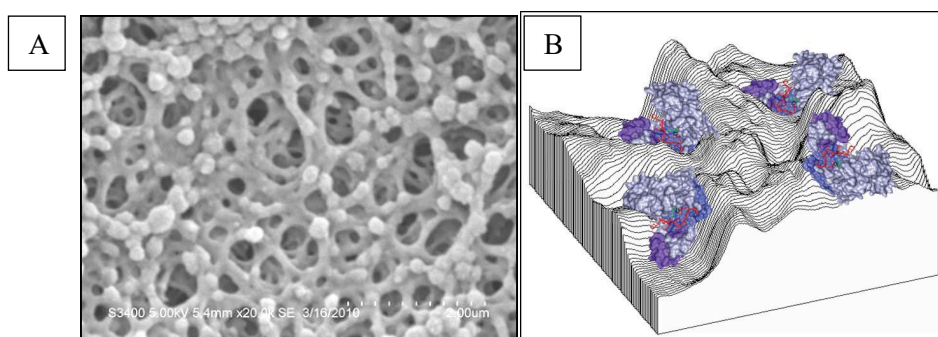


Figure 11. A) Scanning electron micrograph (20,000x magnification) showing the 3-dimensional structure of ONCYTE films, B) Depiction of the 3-dimensional surface.

The related operation manual suggests maintaining the support wet (humid chamber)⁸¹. SA had the surface functionalized with NH₃ amine groups, which brought a positive charge to the surface (Fig.12).

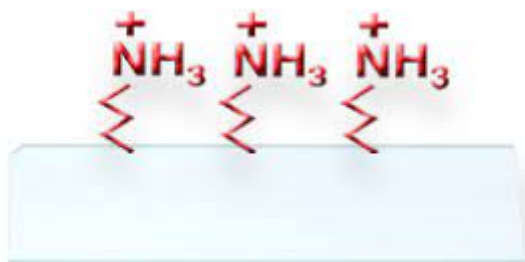


Figure 12. Positively charged amine surface.

The density of the reactive groups is 1×10^{12} per mm^2 . Therefore, the proteins in the solution bonded on the support by electrostatic interaction. The functionalization of these improved the precision, and the slides were used for research in genomic, proteomic, diagnostics and other applications. This support did not require a particular treatment⁸². Sometimes we needed to create hydrophobic barriers on the SA slide to delimit the area of interest, for this purpose we used the Mini PAP Pen (Invitrogen, 75803198A).

2.1.2 Buffer solutions to stabilize the sample droplets

Concerning the tests for producing tiny and repeatable droplets by p-jet with PS, it was planned to use different mixing buffers for testing the effect of different surface tensions on the droplet formation. The buffers investigated were Glycerol, TWEEN 20, TRITON 100x, Dimethyl Sulfoxide (DMSO) and the Protein Microarray Reaction buffer, supplied by the ArrayIt. The surfactants such as TWEEN20 are often used as stabilizers⁸³. Glycerol, TRITON100x and DMSO were often added for the best printing performance⁸⁴. DMSO was added to the printing sample to reduce evaporation of the solution, which had a huge impact on the concentration of the sample during the jetting process. Protein Microarray Reaction buffer was an ultra-pure reagent used for buffer formulation to promote strong signal intensities and high binding specificity. These buffers were used diluted in dH₂O, at different concentrations. With the resulting mixed buffers were performed the different dilutions to test the PS.

2.1.3 Reagents for the reaction support

Background fluorescence sometimes referred to as noise, is the “false” fluorescent signal. Background fluorescence causes can be separated into two main categories:

1. Background fluorescence that is due to the instrument setup and imaging parameters
2. Background fluorescence that is due to autofluorescence of samples, buffers or slides

With the aim at reducing the background signal, and hence maximizing the signal-to-noise ratio (SNR), we tested two kinds of reagents for the reaction support:

- A pre-treatment of the slide before droplet deposition by an *Activation* procedure
- The use of a different kind of *Blocking buffer* after droplet deposition

Protein microarrays such as SuperAmine can be activated before use to improve the protein bond and remove unbound molecules from the surface. The buffers involved in the activation steps were:

- Protein microarray activation buffer (PMAB)
- Protein microarray wash buffer (PMWB)
- Protein microarray rinse buffer (PMRB)

On the other hand, the blocking buffer helped to reduce the non-specific binding of other probe molecules. For this reason, before using antibodies to detect proteins the remaining binding surface had to be blocked to prevent the wrong binding of the antibodies. Proper blocking was imperative for obtaining the best SNR possible from experiments. After different combinations, the blocking solutions supplied by the slide company were the best option.

Test 1

First, the slides were tested for the ability to mark the protein biomarkers. Before using the p-jet method for droplet deposition we performed the very first tests with PS pipetted manually on ONCYTE and SA with a relatively large range of concentrations:

- 2mg/ml,
- 1mg/ml,
- 0.8 mg/ml,
- 0.4 mg/ml,
- 0.25 mg/ml,
- 0.1 mg/ml,
- 0.05 mg/ml

These solutions were diluted in dH₂O. The reaction support of SA was incubated for 18h at 4°C, while the ONCYTE was 3h at 3°C. After the ARS the fluorescent spots were detected by Innoscan,

a confocal fluorescence scanner (see in the Material section for more detail), thus demonstrating the protocol's ability to label the protein. Figure 13 shows the typical scanner images.

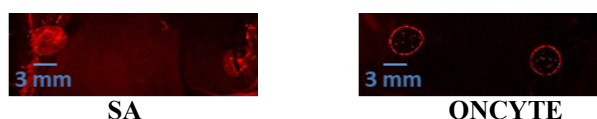


Figure13. Typical scanner images of PS [0.05 mg/ml].

It is important to note that the poor quality of the spots in Fig.13 is due to the manual pipetting procedure. In fact, these first tests allowed one just to select which of the two slides produced the higher intensity in average, thus attributable to a higher binding efficiency. The results showed that the SA slide produced a higher FL intensity on average at a fixed sample concentration and therefore was selected for the successive experiments.

Test 2

To improve the stability and reproducibility of the p-jet spots, different parameters were investigated, such as the spot diameter, the intensity of fluorescence and the signal-to-noise ratio (SNR). The PS at 50 $\mu\text{g/mL}$ was associated with the buffer mentioned in paragraph 2.1.1, to also investigate their effects on the immunoreaction protocol. The incubation of the slide, after deposition, was extended to 18 h 4 °C. The final concentration of A β 1-40 was obtained by diluting the initial solution [2 mg/ml] with the buffers at different concentrations in dH₂O:

- 1% and 10% Glycerol;
- 10% and 0.04% Tween 20;
- 0.5% and 0.04% Tryton 100x;
- 1% DMSO;
- 50% PMRB

The results that were obtained were classified for Diameter, Intensity and SNR, the main parameters of interest. The diameter with the p-jet approach was crucial. In fact, to concentrate the biomarkers dispersed in very low concentration in the sample solution, depositing the micro-droplets in a micro-area was the key to improve the FL signal, and, consequently, the SNR.

Table1 summarizes the main results obtained.




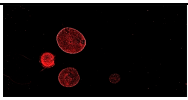
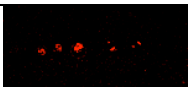
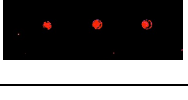
Solution	<Diameter> (μm)	<Intensity> (a.u.)	<SNR>	Innoscan image
Glycerol	-	No signal	-	
Tween	-	No signal	-	
Triton	-	No signal	-	
PMRB	2260,92	544,28	1,93	
DMSO	806,05	16,871	0,563	
dH₂O	288	544	19,75	

Table1. Typical Innoscan images and MAPIX data analysis.

For all mixing buffers, we obtained poor signal intensity, poor spot homogeneity and spot diameter larger than 100 μm . Therefore, the PS was prepared simply in distilled water for the successive tests.

Test 3

To obtain the best diameter and to improve the intensity and the SNR of the p-jet spots, dedicated buffers were tested to pre-treat the reaction support before droplet's deposition. These solutions are intended to improve the protein binding on the slide. The activation of the reaction support aims at increasing signal strength by reducing the background level and by removing unbound protein molecules from the surface. The concentration of PS solution was fixed at [50 mg/ml]. The activation steps were performed by incubating the PMAB for 1h at 15°-25°C on a shaker. The slide was then washed 5 min with PMWB and 1 s with PMRB at 15°-25°C. Table 2 reports the data obtained by MAPIX software and a comparative analysis between activated and not activated support.

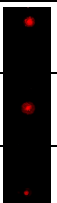
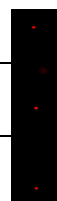
	Diameter (μm)	Intensity (a.u.)	SNR	Image
Activated	380	1187	6	
	450	743	31	
	175	608	6	
No-activated	100	3092	450	
	100	4667	526	
	90	2054	196	

Table 2. Typical scanner images (last column right) and measurements obtained in test 3 by MAPIX tool.

The best results were obtained in case of not activated support, where the diameter of the spots was shorter, concentrating with more efficient the biomarker's droplets, and both intensity and SNR were higher. Therefore, the successive tests were performed on not activated slides.

The list below summarizes the protocol conditions fixed after the tests reported above:

- Slide reaction support adopted was SuperAmine
- The support did not pre-activated before the jetting
- The deposition with p-jet of the PS was performed without mixing the solution with other buffers, incubating the biomarker solution 18 h 4°C
- After the incubation was deposited on the reaction support the blocking solution of the SA slide company
- The washing steps and primary and secondary antibody reaction were performed following the datasheet suggestions

In this way, the protocol was 3 days long:

day1 -> deposition

day 2 -> blocking and primary antibody incubation

day 3 -> secondary antibody reaction and fluorescence acquisition

Test 4

The above mentioned protocol conditions were then tested for the more complex A β 1-42 protein, that we call PS2 for brevity.

Table 3 reports the typical results obtained by this approach on the following concentrations: 50 μ g/ml, 50 ng/ml and 500 pg/ml.

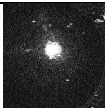
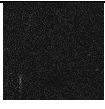
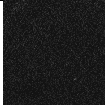
PS2 concentration	Diameter (μ m)	Intensity (a.u.)	SNR	Image of one spot
50 μ g/ml	110	8.374	14	
	110	15.880	23	
	110	7.572	10	
50ng/ml	110	72	0	
	110	28	0	
	110	39	0	
500pg/ml	110	45	0	
	110	17	0	
	110	54	0	

Table3. Results obtained with PS2 adopting the protocol explained in Test 3.

This purely qualitative test shows how the conditions used for the PS immunoreaction were not compatible for the PS2. The A β 1-42 instability compared with A β 1-40 brought us to reevaluate the protocol conditions.

Test 5

To reduce the duration of the protocol and to check the possibility to improve the SNR shown in the previous section, the protein incubation was shortened from 18h at 7°C to 2h at 25°C, keeping the concentrations fixed.

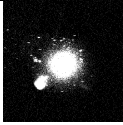

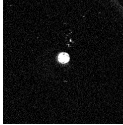
PS2 concentration	Diameter (μm)	Intensity (a.u.)	SNR	Image of one spot
50 μg/ml	110	23.232	22	
	110	11.075	15	
	110	859	3	
50ng/ml	110	5.288	8	
	110	991	3	
	110	497	3	
500pg/ml	110	1.788	18	
	110	1.055	8	
	110	149	1	

Table 4. Typical scanner images and Mapix outcomes in case of test 5.

These results show qualitatively how the protein incubation has a significant role in the immunoreaction protocol. In conclusion, after these preliminary tests, the protocol steps were fixed according to the following table 5.

STEP TITLE	TIME	TEMPERATURE	HUMIDITY
Preparation of the sample		Ambient (around 25°C)	Ambient (around 40%)
Spotting by p-jet on the SuperAmine glass reaction slide		Ambient (around 25°C)	Ambient (around 40%)
Incubation of the protein	120 min	Ambient (around 25°C)	Wet chamber (around 80%)
Incubation with blocking buffer	60 min	Ambient (around 25°C)	Ambient (around 40%)
Washing on the shaker	3 X 5min	Ambient (around 25°C)	Ambient (around 40%)
Incubation with primary antibody	18h	Fridge (around 7°C)	Wet chamber (around 80%)
Washing on the shaker	3 X 5min	Ambient (around 25°C)	Ambient (around 40%)
Incubation with the secondary antibody	60min	Ambient (around 25°C)	Wet chamber (around 80%)
Washing on the shaker	3 X 5min	Ambient (around 25°C)	Ambient (around 40%)
Reading	-	-	-

Table 5. Summary of the protocol steps.

Chapter 3 Materials and methods

3.1 Lithium niobate and the pyroelectric effect

The p-jet technique used in this thesis work was based on the pyroelectric effect and on the use of ferroelectric crystals (i.e. lithium niobate, LN) with pyroelectrically generated electric fields. LN is a rhombohedral crystal. Thanks to its unique optical, electronic, and physical properties, LN finds applications in different fields such as nonlinear optical devices, compact pyroelectric sources of x-rays, piezoelectric resonance biosensors, just to cite some. The main obstacle in the way of its developing industrial, caused by expensive high-quality mechanical elaboration of LN samples, is currently reduced due to implementation of micromachining CNC (Computer Numerically Controlled)⁸⁵ and laser micromachining techniques⁸⁶. The LN crystals were bought from Crystal Technology Inc. in the form of both sides being polished c-cut LN 500 μ m thick, with a diameter of 3 inches. A standard diamond saw was used to retrieve 2 x 2 cm² samples. The spontaneous polarization P_s of the LN crystal changes according to $\Delta P_s = p \Delta T$, where p is the pyroelectric coefficient and ΔT is the temperature variation ($p = -8.3 \times 10^{-5} \text{ C m}^{-2} \text{ K}^{-1}$ at $T = 298 \text{ K}$). At equilibrium conditions, the spontaneous polarization of the LN crystal is shielded by the external screening charge, without the electric field generation (fig. 5a). When the crystal is stimulated through a temperature variation, a surface charge density $\alpha = p_i \Delta T$ appears locally due to uncompensated charges. A high electric field ($E_{NL} 10^7 \text{ V/m}$) is generated on the surface of the LN crystal (fig. 5b). Therefore, as well explained in previous works^{61–63}, the spontaneous polarization P_s changes according to $\Delta P_i \propto p_i \Delta T$, where P_i is the coefficient of the polarization vector, p_i is the pyroelectric coefficient and ΔT is the temperature variation ($p_i = -8.3 \times 10^{-5} \text{ C m}^{-2} \text{ }^\circ\text{C}^{-1}$ for LN at 25°C). Taking advantage of this feature, the pyro-electric field applied to a liquid drop can lead to a redistribution of the mobile charges in the liquid sample. When sufficiently strong, the electric field deforms the sample droplet and forms a conical tip from which tiny droplets are released.

3.2 Slides

Because of the preliminary tests shown in the paragraph 2.1.2, in the immunoreaction protocol, the reaction support chosen was the slide functionalized with the ammino groups NH_3^+ Arrayit SuperAmine 2 Ultra Low Density (Cat. SMM2ULD). The proteins were bound electrostatically on the surface with its charged backbone, in this reaction intervened non-covalent bond. In the case of the fluorescent probes used in the tests, we used standard 1 mm thick microscope glass slides.

3.3 A β 1-42 protein solution for immunoreaction

The AD biomarker A β 1-42 (Sigma Aldrich, AG912) was bought as white lyophilized powder and resuspended in 1% Ammonium hydroxide solution (NH_4OH) (Sigma Aldrich, 221228) at a concentration of 1 mg/ml according to manufacturer procedures. Afterwards it was sonicated for 30 s and stored undiluted at -20°C . The serial dilutions were prepared with PBS1X to obtain the final concentrations at 100 pg/mL, 20 pg/mL, and 4 pg/mL.

3.4 A β 1-42 protein solution for rheological characterization

The white lyophilized powder of A β 1-42 ((Sigma Aldrich AG912) was resuspended in 2 mM of NaOH so that a stock solution was obtained (1 mg/ml) according to datasheet, and then sonicated for 45 s. The serial dilutions were prepared with PBS1X (Gibco 10010023) to obtain four aliquots of each final concentration at 800 μ g/mL, 400 μ g/ml, and 40 μ g/mL. The aliquots were stored at -20°C. On the day of use, the aliquots of interest were thawed. To ensure the same frozen-thawed process for all solutions measured, on day 0, namely the reconstitution day, an aliquot of 800 μ g/mL, 400 μ g/ml, and 40 μ g/mL was frozen and thawed before the measurements.

3.5 Fluorescent probes

Two kinds of fluorescent probes were used: 1) Alexa Fluor 647 (far-red-fluorescent dye, cat. no. A33084, life technologies); 2) secondary antibody conjugated with Alexa Fluor Plus 647 (cat. no. A32733, life technologies). The fluorophore was bought as a powder and dissolved in 1X Phosphate Buffered Saline (cat. No. 10010023, life technologies), at a concentration of 1.25 mg/ml. The solution was mixed gently to ensure the solubilization of the powder. Starting from this solution, 20 μ l, 9.6 μ l, and 5 μ l were diluted in 2 mL of PBS (Phosphate-buffered saline) 1X, each one, to have the final concentrations of 12.5 μ g/mL, 6 μ g/ml, and 3 μ g/mL. The secondary antibody was bought as a solution with an initial concentration of 1 mg/mL and diluted in dH₂O at the final concentrations of 10 pg/mL, 0.1 pg/mL, and 0.01 pg/mL.

3.6 Immunoreaction protocol

The immunoreaction protocol was performed by following the steps described in Table 5. The A β 1-42 was deposited by using the p-jet technique, afterwards, the slide was incubated in a humid chamber for 2 h at 25 °C. For saturating excess protein-binding sites, the slide was covered with 2 mL of ArrayIt Blocking solution (BlockIt Blocking buffer) for 1 h at 25 °C. The blocking solution was used to dilute the antibody solutions. Then the slide was washed by placing it in a Petri dish with 10 mL of PBS 1X (Gibco 10010023) for 2 min. This washing cycle (WC) was repeated three times. A solution of primary antibody (AbI), 2mL of rabbit anti- β -Amyloid 1-42 (Cell Signaling Technologies Rabbit, D9A3A) at the dilution of 1:1600 was deposited on the slide and incubated overnight at 4°C. The WCs were repeated. Finally, the secondary antibody (AbII) solution (Thermo Fisher Scientific anti-Rabbit I, A32733), at the concentration of 0.5 μ g/mL, was incubated for 1 h at 25 °C and the WCs were repeated.

3.7 Fluorescence acquisition and analysis

The scanner used in the fluorescence analysis was the InnoScan 710 (see the picture in Fig.14). The InnoScan is a confocal fluorescence scanner. The imaging system has two laser sources to excite the

chemifluorescent dyes at wavelengths 635 nm and 532 nm. Two detection photomultipliers and very high-precision optical filters provide results with enhanced SNR.



Figure 14. Innoscan 710 image

We operated at 635 nm wavelength to read our AbII signal. The laser sources had controlled temperature and current, to avoid possible imbalances able to damage the samples. Depending on the expected spot size and signal intensity, four main scan parameters can be adjusted: resolution (from 3 to 40 $\mu\text{m}/\text{pixel}$), scanning speed (from 10 to 35 lines/s), gain PMT (linear from 0 to 100 %), laser power (5 and 10 mW). The TIFF 16-bit images captured by the scanner were evaluated quantitatively by MAPIX software. MAPIX is a high-performance and easy-to-use microarray image analysis software, which allows one to measure the signal intensity in the selected spot areas. Figure 15 shows the MAPIX user-interface where the operator can set the scanning parameters.

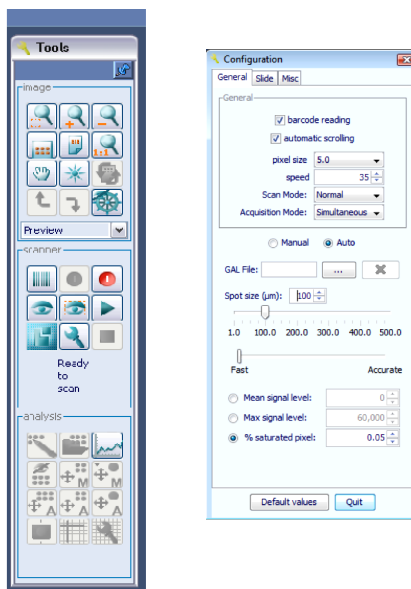


Figure 15. Typical MAPIX user interface where the operator selects the scanning parameters.

3.8 The piezo-driven biospotter

The performance of the p-jet accumulation was compared to a commercial piezo driven biospotter (S3 sciFLEXARRAYER, Scienion AG) using a set of fluorophore samples. S3 is a non-contact dispensing system designed to produce small sample spots from ultra-low volumes of biomaterials. Samples were dispensed on top of low auto-fluorescence glass microscope slides (Marienfeld, ref.

1010200) after a washing procedure, where the slides were first rinsed with acetone and isopropanol, and then dried with nitrogen blow (Topgun). Fluorophore samples were prepared by diluting Alexa Fluor 647 carboxylic acid tris(triethylammonium) salt (A33084 Invitrogen) in 12 mM PBS (pH7,4) to achieve fluorophore concentrations for three ranges: (1) 0.01 pg/ml to 10 pg/ml, (2) 10 ng/ml to 1 µg/ml and (3) 3 µg/ml to 12.5 µg/ml. The dispensed individual drop size with S3 was 350-372 µl and distance between the nozzle and the sample slide was 282-500 µm. Three replicate sample slides were prepared for the three concentration ranges.

3.9 The pendant drop tensiometer

A pendant drop tensiometer (First Ten Angstroms FTA 1000) was used for the surface tension measurements (see Fig. 16). It is a modular video drop shape system, composed by the following main components:

- backlight source
- microscope optics
- video camera connected to a computer
- liquid dispense pump
- support stage

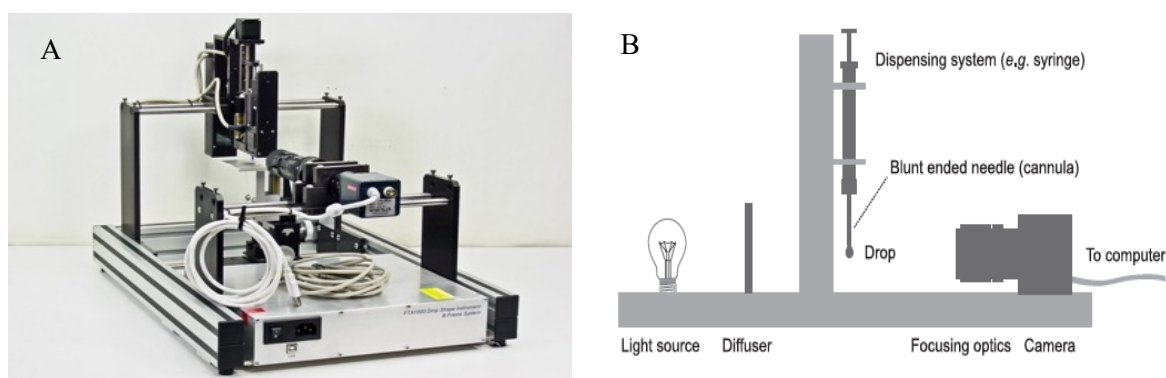


Figure 16. A) Picture of a typical tensiometer FTA100; B) schematic view of the main components of the FTA1000.

The backlight source is a specialized illumination with a 25 mm blue LED, positioned behind the drop sample. The image is recorded by a digital camera equipped with a microscope objective (0.7X to 4.5X of magnification). The camera is connected to a computer for analyzing the data by using the software FTA 32 Video 2.1.

The dispensing system is composed of a syringe with a volume of 250 µl to 26 nl and a needle from which is formed the drop, and an automated pump with a pumping velocity of 0.02 µl /s to 5 µl/s that controls the fluid release and the drop formation (see Fig. 17).

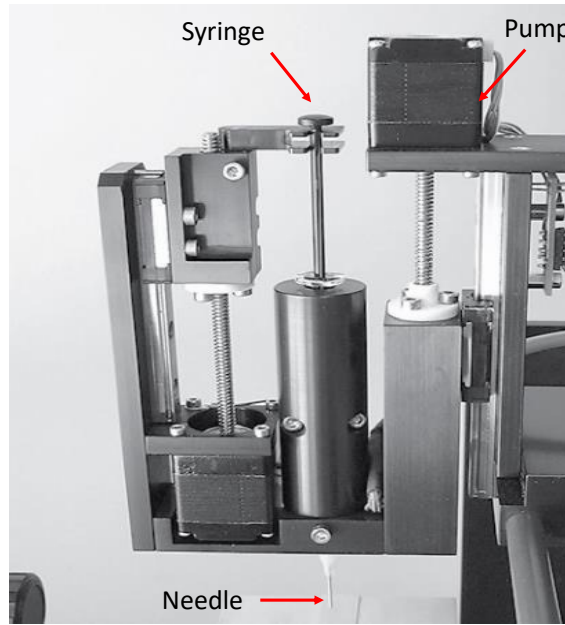


Figure 17. Picture of the dispensing system, with main components indicated by the red arrows (needle, syringe, pump).

The surface tension measurements were performed by the Drop Shape Method⁸⁷. The analysis is based on two principal assumptions, the drop is symmetric about a central vertical axis and surface tension and gravity are the only forces shaping the drop. Young-Laplace equation allows one to establish the surface tension by fitting the shape of the drop (in a captured video image) with the relates interfacial tension to drop shape⁸⁸(Fig.18). The shape of a drop is determined by its radii of curvature, R_1 and R_2 . In the case of a spherical drop, these are the same. The radii are defined according to Adamson et al⁵⁴. The relationship between interfacial pressure (the pressure across the interface) and these radii of curvature is called the Young-Laplace equation⁸⁹:

$$\Delta P = \Delta \left(\frac{1}{R_1} + \frac{1}{R_2} \right) \quad (1)$$

Where ΔP is the interfacial pressure difference, γ is the interfacial tension, R_1 , R_2 are surface's radii of curvature. In a column of fluid of density ρ and height h ,

$$\Delta P = \rho gh \quad (2)$$

and g is the acceleration due to gravity, (9.8m/s^2). The software performs these steps automatically. Moreover, it is important to note that the drop image has to be recorded with highest focus quality as possible, to obtain more accurate measurements.

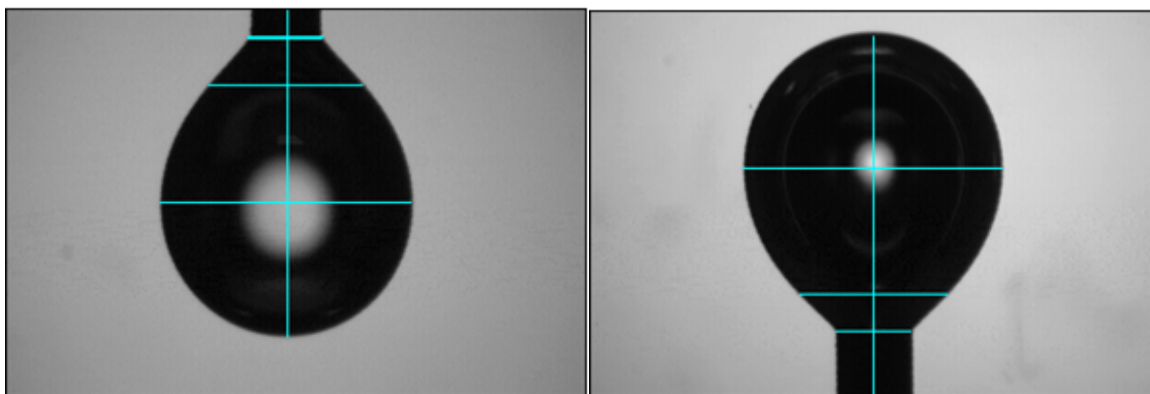


Figure 18. Typical drop image with central vertical axis overlapped.

3.10 Sample interfacial tension measurements

The sample interfacial tensions (IFTs, γ) were calculated during the time, following the evolution of them⁹⁰. The IFTs of protein solutions were determined by using the tensiometer (First Ten Angstroms FTA 1000) equipped with software (FTA 32 Video 2.1). The measurements were performed at room temperature ($24 \pm 1^\circ\text{C}$) during 2400 s, acquiring the data every 2 s, for each solution in triplicate. The protein solutions, dissolved and storage as mentioned, were used in the measurements at different times during a period of 30 days after the protein package opening: freshly dissolved protein solution (day 0), after one week (day 7), after two weeks (day 14), and after 1 month (day 30). The protein solutions of A β 1-42 were investigated at three concentrations: 800 $\mu\text{g/mL}$, 400 $\mu\text{g/mL}$, and 40 $\mu\text{g/mL}$. More details about the solution are included in section 3.4.

3.10.1 Preliminary tests and definition of the measurement protocol

To perform an accurate measurement, the droplet stability and the volume had to be preserved. In case of open space conditions, the data collected appeared to underline a significative correlation between a variation of volume with IFT (Fig. 20B). For this reason, a homemade closed system (HCS) was implemented to ensure a controlled space, as shown in Figure 19.

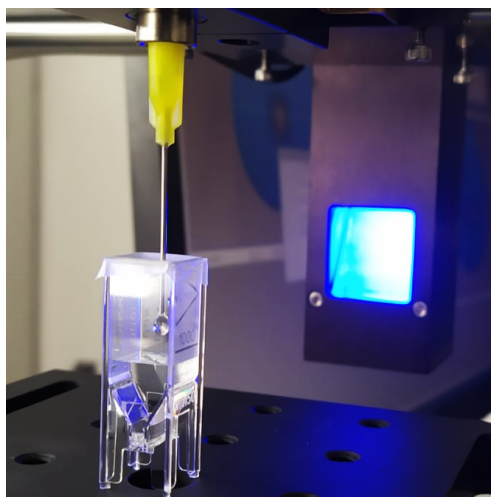


Figure 19. Picture of the homemade closed system for the pendant drop.

The HCS was composed by a conventional polystyrene cuvette (Eppendorf® UVette®, Sigma-Aldrich) sealed by a piece of Parafilm (Parafilm PM996, Sigma-Aldrich). The Parafilm layer was perforated before insert the needle connected to the dispensing system. The cuvette appeared a convenient way for protecting pendant drops from air currents and, therefore, for reducing the evaporation rate. In fact, the cuvette was filled by 500 μL of dH_2O , to guarantee an appropriate level of humidity such as to have a saturated environment and, therefore, a significant decrease of the evaporation rate. The tensiometer provides reliable measurements for drop volumes $\geq 10\mu\text{L}$ ⁸⁷. Therefore the pendant drop volume (PndVol) was set at 15 μL . Calibration measurements were performed first, to evaluate the role of the cuvette. The PndVols and the IFTs of distilled water were measured for 55 min with and without the HCS and the results are reported in Fig. 20.

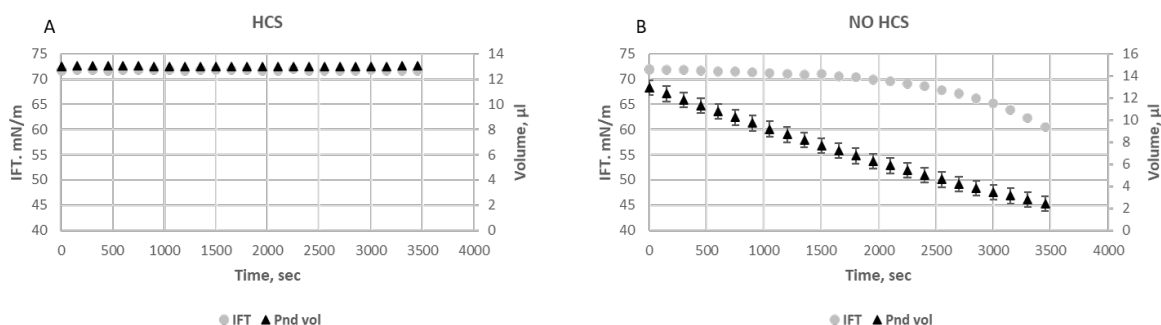


Figure 20. Calibration tests, with volume variation: A) with HCS; B) without.

These results demonstrate the reliability of the measurements under HCS conditions. The calibration tests were performed comparing the IFTs value of the dH_2O reported in literature, 71.99 mN/m at 25°C with an acceptable error of 0.3% and 0.7% respectively⁹¹, with the data obtained. In fact, the data showed the IFTs of distilled water of 72.02 mN/m \pm 0.2 without the HCS and 71.85 mN/m \pm 0.3 with the HCS. The PndVols recorded with the HCS remained constant at a value of 15 $\mu\text{L}\pm$ 0.1. Conversely, the test performed in open space, the PndVol decreased with a variation of 81.18%. For this reason the HCS was used for the IFTs measurements.

3.10.2 Mathematical models

In the adsorption process of proteins at an air/water interface, the proteins could follow these steps:

- 1) diffuse from the bulk towards the interface,
- 2) adsorption/penetration at the interface,
- 3) molecular rearrangement^{92–96}.

These steps are shown in Figure 21⁹⁷.

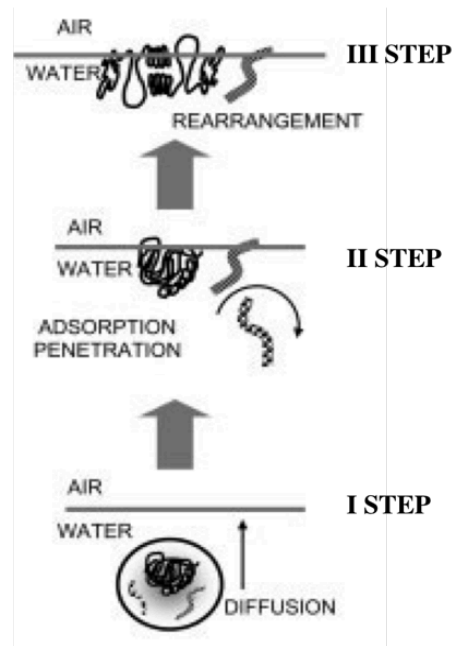


Figure 21. Proteins diffusion from the bulk to interface.

The first step, related to the diffusion, is described by the Ward-Torday equation⁹⁸ [Click or tap here to enter text.:](#)

$$\pi = \gamma(t) - \gamma(0) = C_0 K T \frac{D_{diff} t}{\Pi} \quad (3)$$

Where π is the interfacial pressure at any time, $\gamma(t)$, $\gamma(0)$ are the surface tension at any time t and at time zero respectively, C_0 is the bulk concentration in the aqueous phase, K is the Boltzmann constant, T is the absolute temperature, D_{diff} is the diffusion coefficient, Π is the Pi greco value⁹⁸ π as a function of $t^{1/2}$ is possible to obtain the diffusion rate (k_{diff}) as the slope of the curvature⁹⁶

$$k_{diff} = C_0 K T \left(\frac{D_{diff}}{\Pi} \right)^{1/2} \quad (4)$$

The second and the third steps are described with the Graham and Philips equation⁹⁹ [Click or tap here to enter text.:](#)

$$\ln \frac{(\pi_f - \pi_t)}{(\pi_f - \pi_0)} = -k_i t \quad (5)$$

where π_f, π_t, π_0 are the surface tension at the end of the adsorption processes, at any time and at $t=0$, respectively. k_i is a first-order constant. The application of equation (5) can identify two linear regions with two different slopes. The first one is related to proteins adsorption, while the second one is related to the rearrangement of the adsorbed proteins. As a result, two different constants (k_{ads} and k_r)^{92,94–96}.

3.11 Determination of the fluorescence intensity

To compare the molecular rearrangement with the antibody capability to recognize the proteins during the 30 days when they had the right conformation, it has been performed the immunoreaction protocol on the same concentration tested for the IFTs: 800 µg/ml, 400 µg/ml, and 40 µg/ml. Four droplets for each Aβ1-42 solution were deposited with a traditional pipette in the volume of 3 µl on the glass slide functionalized with 2D-Amine groups (see section 3.2). The immunoreaction protocol was reported in detail in Section 3.6, while the FL signal intensity was evaluated by using the Innoscan710 and analysed by MAPIX software, both described in section 3.7. The scanner was set with the laser source at 635 nm for exciting the fluorescent molecules, the resolution was set at 10 µm/pixel, the speed was 35 lines/s, the gain of the PMT was 5% and the laser power was 5 mW. The TIFF 16-bit images captured by the scanner were evaluated quantitatively by Mapix software.

3.12 Statistical Analysis

The kinetic constants K_d , K_{ads} and K_r of the concentrations 40 µg/ml, 400 µg/ml and 800 µg/ml were calculated at day0, day7, day14 and day30 through the mathematical models explained in section 3.10. In particular, to understand if during the time the kinetic constants were subject to a significant changed, statistical analysis was applied to correlate the value obtained in the days. The dependent variables were the constant values, while the days were considered the qualitative variable. The first steps were assessing the assumption of normality with the *Shapiro-Wilk test*, the test verified the normal distribution of the data, obtaining in each case $pvalue > \alpha$. Therefore, it was adopted the parametric test *One-Way ANOVA*. In this way it was possible to compare the means of the kinetic constants during the days. The Fisher's F test obtained reflected the probability corresponding to the F value, with $Pr > F$ value that determined the significance of our results. Once ANOVA found the significant difference, a post hoc test were selected, the *Dunn's Multiple Comparison test*. This helped the operator to evaluate the significative differences between which groups have been evidenced. The tests were performed by Excel (version XLSTAT 2022 3.1.1338.0)

Chapter 4 Results and discussions

4.1 Reproducibility of the p-jet spots

The p-jet technique was tested for accumulating diluted biomolecules^{63,69} and make them detectable even down to sub picogram levels of concentrations. In the last years, the possibility of using the pyroelectric effect for accumulating micro-droplets and for detecting highly diluted biomolecules was demonstrated for the first time. Here, a completely new configuration was presented where a more compact and easier-to-use heating system was developed, compared to the CO₂ laser head or to the μ -heater used in the previous papers. This advanced experimental setup, as well as the thermal stimulus for generating the pyroelectric effect, were thoroughly described in Sections 2.3 and 2.5. The reproducibility of the spots generated by this new p-jet configuration was evaluated by printing around 100 replicates of spots obtained by delivering 1 to 5 droplets and 10 to 50 droplets at each position. The successive droplets are indicated here as jets, for brevity. The sample was the Alexa fluorescent probe (see Materials and Methods) at a concentration of 6 $\mu\text{g/mL}$. Soon after the delivery of one spot, the target slide by 1 mm with the precision translation stage was translated, then with successive spots was proceeded. Figure 22 shows a typical scanner image of the resulting spots, just as an example.

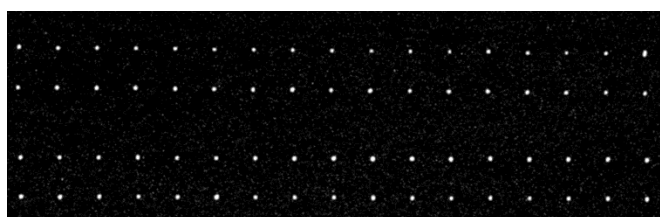


Figure 22. Scanner image of the typical p-jet spots obtained by spotting droplets of Alexa fluorescent probe.

The recorded scanner images were analysed by Mapix software. The diameter of the spots was on average 75 μm with a coefficient of variance of 5% for spots with 1-5 jets and 130 μm with a coefficient of variation of 7% for the spots with 10-50 jets. Therefore, the variation of spot diameter was negligible with the increasing number of jets in both ranges, and the FS data were analysed indifferently through 'F tot' or 'F mean' in the case of the p-jet spots. In fact, the first represents the sum of the gray values of all the pixels in the spot area and the second is F tot divided by the number of pixels in the spot area. In other words, the F mean values give information about the optical density of the spots. The FS had a variability of around 6% for the different groups of replicates at the same number of jets. These results demonstrate the significance of the data and the high repeatability of the p-jet spots in terms of both diameter and FS.

4.2 Characteristic curves of the p-jet accumulation

To test the reliability of this new p-jet sensor for tuning the accumulation rate of low abundant biomolecules, the behavior of the FS of the spots as a function of the number of droplets (referred to as jets) delivered for each spot was evaluated. It is well known that ELISA-based procedures represent the gold standard in most clinical diagnoses aimed to detect specific biomarkers in human fluids. Detection of A β 1-42 in human cerebrospinal fluid for Alzheimer's disease diagnosis is challenging for ELISA having the LOD of 50 pg/mL, which prevents a reliable detection of these biomarkers in peripheral fluids such as blood, where the concentrations are expected to reach only sub-picogram levels. Considering the novelty of the technique, this study was performed first for three relatively high concentration values in the μ g/mL range (12;6;3) and successively for three challenging concentrations less than the ELISA LOD mentioned above (10 pg/mL; 0.1 pg/mL; 0.01 pg/mL).

The pin with the Alexa probe sample at 12.5 μ g/mL was loaded, and five spots were printed, the first with one jet and the others by accumulating two jets, three jets, four jets and five jets, respectively. Eight replicates for each spot were performed, and the same kind of experiment for the other two concentrations at 6 μ g/mL and 3 μ g/mL was repeated. Figure 23 shows the behavior of the FS as a function of the number of accumulated jets for the three concentrations at the μ g/mL level.

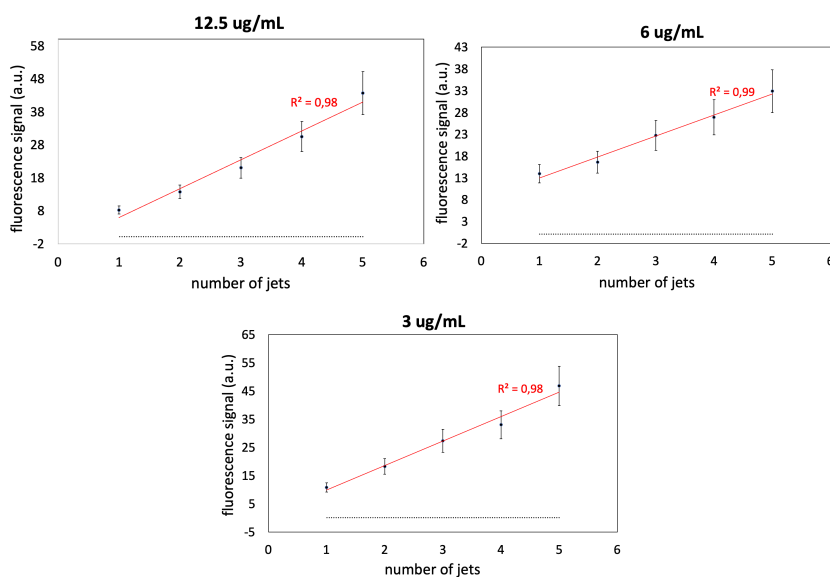


Figure 23. Fluorescence signal of the p-jet spots as a function of the increasing number of jets, for three concentrations of the Alexa probe. The signal values were averaged on eight replicates of the spots and the error bars correspond to their standard deviation. The linear plots were obtained by least squares fitting. The horizontal dashed lines correspond to the background level calculated as three times the standard deviation of the background FS.

The dashed lines correspond to the background level calculated as three times the standard deviation of the background signal. The data on the Y axis corresponds to the average FS over eight replicates of the spots calculated as mean gray values per unit area of the spots. These results show that the

optical density of the spots increased linearly with an increasing number of accumulated jets for each concentration, and the linear regression equations exhibited $R^2 \geq 0.98$.

After appropriate cleaning of the printing pin, the labeled antibody probe solution (see Materials and Methods) at the concentration of 10 pg/mL was loaded and ten spots with an increasing number of jets from one to ten were printed. On the same target slide, ten spots were deposited by simply touching the slide with the printing pin from one to ten times for each spot. We performed three replicates of the spots, and the fluorescence images of the slides by the scanner was recorded. The images were analyzed by Mapix and the resulting data were averaged over three replicates. **Fig.24(a)** shows the corresponding graph.

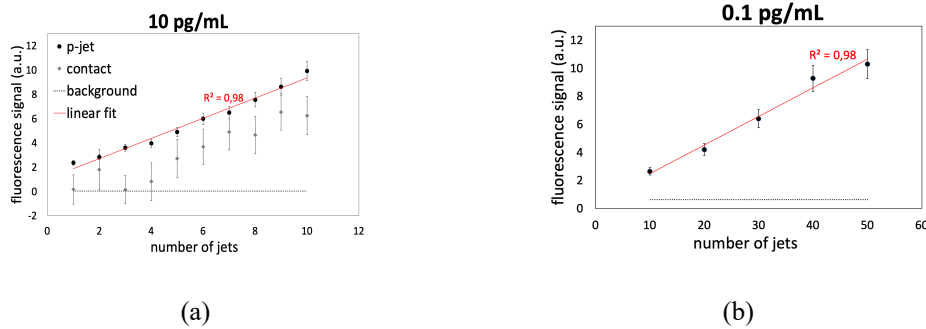


Figure 24. Fluorescence signal of the p-jet spots for an increasing number of jets of the labelled antibody sample in case of (a) 10 pg/mL; (b) 0.1 pg/mL. In (a) we also report the results in case of 10 pg/mL by contact printing. Error bars represent their standard deviation resulting from three replicates of the spots. The linear plots were obtained by least-squares fitting. The horizontal dashed lines correspond to the background level calculated as three times the standard deviation of the background signal.

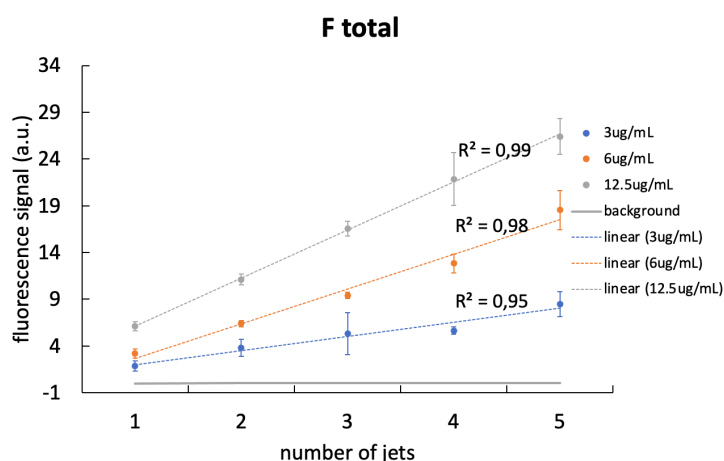
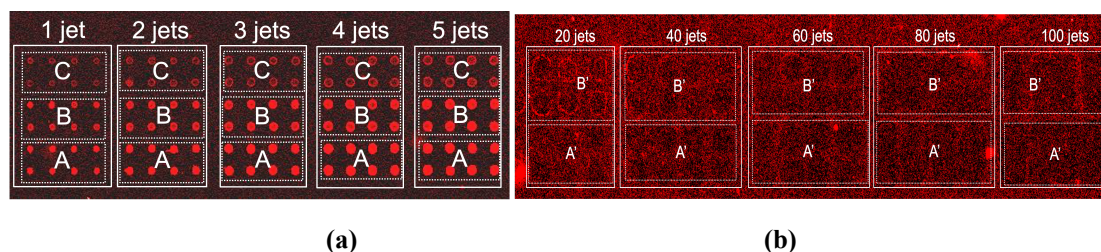
The results in **Fig.24(a)** demonstrate clearly that the contact-based accumulation does not behave linearly over the range of 1-10 touches, due to the cross-contamination occurring in successive touches of the pin on the same spot location. Moreover, the contact nature of this print method also means that during every deposition there is a chance that the pin tip may be damaged, thus worsening the repeatability in the deposited volume at each touch^{58,100}. The lack of reliability was evident also through the behavior of the FS in the spots obtained with a few touches, where the signal is not detectable significantly over the background level. Conversely, the FS of the spots obtained by p-jet accumulation at 10 pg/mL is significantly higher than the background level, even for a few jets with an average signal/noise ratio (SNR) of 90 at one and two jets. Analogously to the case with the Alexa probe, also in this case the data show that the optical density of the spots increased linearly with the increasing number of accumulated jets, with linear regression equations exhibiting $R^2 \geq 0.99$.

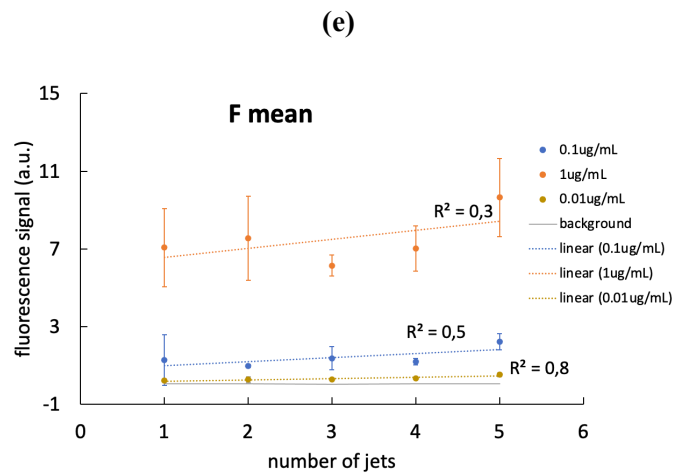
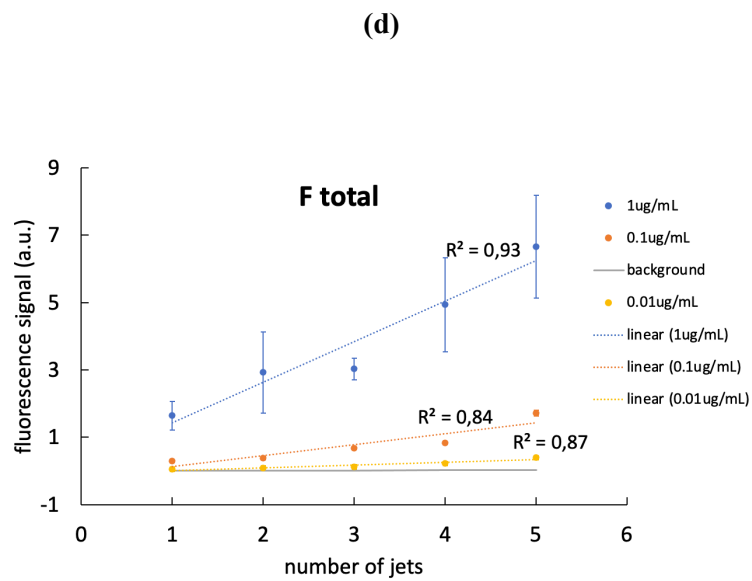
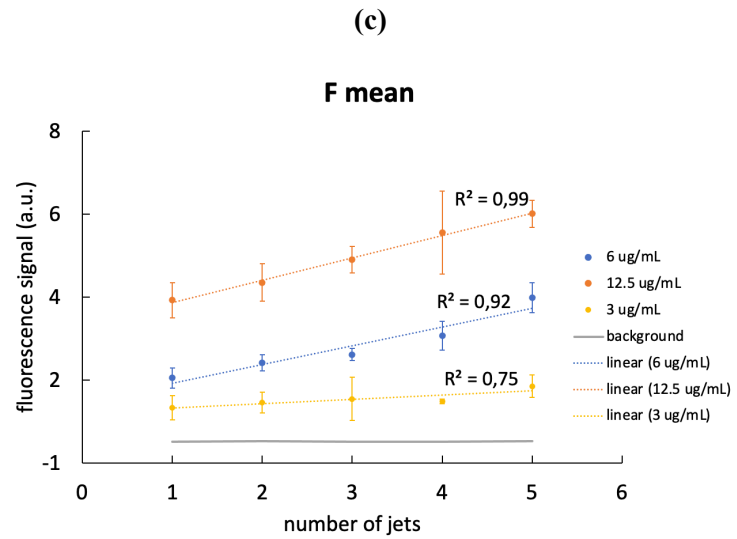
The same kind of characterization was performed for 0.1 pg/mL to test the reliability of the p-jet accumulation at very challenging levels of concentration. Considering the two and three orders of magnitude decrease in concentration the accumulation effect by using a higher number of jets, from 10 to 50 at a step of 10 was tested. Three replicates of the spots also in this case were performed and

the fluorescence images of the slides by the scanner were recorded. The images were analyzed by Mapix and the resulting data were averaged over the three replicates (see **Fig.24(b)**). The SNR ranged from 6 to 14 and the spot optical density increased linearly in the whole range of jets. These results demonstrate the reliability of the p-jet in tuning linearly the rate of accumulation of biomolecules by the number of jets and in detecting fluorescence-labeled A β 2 proteins at challenging concentrations, thanks to the significant increase of the optical density.

4.3 Comparison with S3 biospotter dispensed samples

The performance of the new p-jet sensor was compared to a commercial piezo spotter S3 biospotter. S3 was used to dispense eight replicate sample spots with one to five dispensed jets at each position. The sample was the Alexa fluorescent probe (see Materials and Methods). The behavior was evaluated as a function of the number of jets for different concentration ranges. The first concentration range included 12.5 μ g/mL - 6 μ g/mL - 3 μ g/mL, the second 1 μ g/mL - 0.1 μ g/mL - 0.01 μ g/mL, the third 10pg/mL - 0.1pg/mL - 0.01pg/mL. The FS was measured by the scanner, and the images were analyzed by the Mapix software. Figure 25(a,b) shows the typical scanner images of the slides with spots at the second and third concentration ranges, respectively. Figure 38a shows that the spot diameter increased significantly with the number of jets, on average from 300 μ m (1 jet) to 600 μ m (5 jets), and Figure 25b shows the lack of significance of the spots at the challenging dilutions. The FS was analyzed here in terms of both F tot and F mean values and Figure 25(c-f) show the corresponding results.





(f)

Figure 25. Biospotter results. (a,b) Typical scanner images of the slides with the spots at 1ug/mL (A), 0.1 ug/mL (B), 0.01ug/mL (C), 0.1pg/mL (A') and 0.01pg/mL (B'); (c,e) F tot as a function of the number of jets for the concentrations in the ranges 12.5ug/mL-3ug/mL and 1ug/mL-0.01ug/mL, respectively; (d,f) F mean as a function of the number of jets for the concentrations in the ranges 12.5ug/mL-3ug/mL and

1 μ g/mL-0.01 μ g/mL, respectively. The data in (c-f) were averaged over eight replicates of the spots with error bars corresponding to their standard deviation. The linear functions were obtained by weighted least-square method. The average diameter in (a) is 300 μ m for 1 jet and 600 μ m for 5 jets.

Both F_{tot} and F_{mean} increase with the number of jets for all the concentration ranges. However, while F_{tot} increases on average by a factor of five and six in the first and second concentration range respectively (see Figure 25(c,e)), the F_{mean} increases only by a factor of two in all samples (see Figure 25(d,f)). This means that the increase in spot optical density is negligible for increasing jets, thus preventing the accumulation effect achieved instead by p-jet. In fact, the spots at challenging concentrations have $SNR < 1$, even up to 100 jets (see Figure 25b). Moreover, linear regressions with $R^2 \geq 0.98$ were achieved only for the F_{tot} values at 12.5 μ g/mL and 6 μ g/mL and for F_{mean} values at 12.5 μ g/mL, thus demonstrating the lack of linear behavior for all the concentrations below the μ g/mL level. These results demonstrated that the accumulation rate achievable through the p-jet sensor is unique and not reachable through a commercial piezo-driven dispensing biospotter, thus launching the p-jet as a new tool for sub-picogram detection of biomolecules.

4.4 Application for immunodetection of A β 1-42

The p-jet sensor was tested for a real application of immune-detection by using the biomarker A β 1-42. It belongs to the family of biomarkers object of clinicians' interest in the diagnosis of AD. This study had attention to a set of concentration values falling in the challenging range of pg/mL. Three spots were produced with 20 accumulated droplets for each concentration value. The spot images were recorded by the scanner and evaluated by Mapix. Figure 26 shows the resulting data averaged over three replicates of the spots.

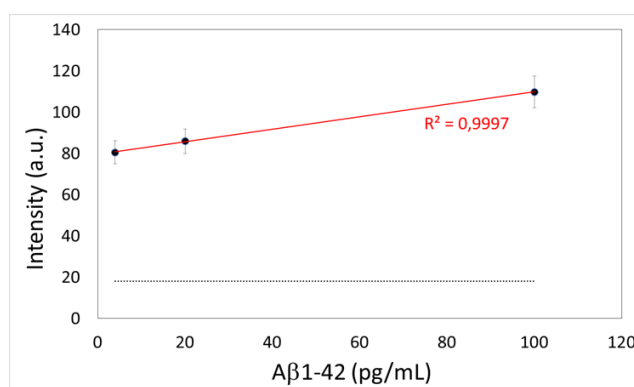


Figure 26. Mean fluorescence intensity of the p-jet spots of A β 1-42 with increasing solution concentration. Error bars represent the standard deviation of three replicated spots. The linear plot was obtained by least-square fitting. The horizontal dashed line corresponds to the background level calculated as three times the standard deviation of the background signal.

These results demonstrate the reliability of the p-jet for detecting A β 1-42 onto a solid surface through an immunoreaction protocol, with a linear behaviour in the pg/mL range of concentrations, below the current limits of traditional ELISA kits. In perspective, this technique would simplify the detection of low abundant biomolecules by accumulating them directly onto the reaction slide and by using sub-microliter volumes of reaction, with significant advantages in all those cases where diagnostic applications must be performed with very small volumes of the analyte. A new p-jet sensor with the ability to enhance the fluorescence signal of low abundant biomolecules linearly by increasing the number of accumulated jets. This technique provides an easy-to-use procedure that can tune the accumulation rate of target molecules in highly diluted solutions. The reliability of the technique has been demonstrated for a fluorescent probe with a concentration falling well below the current limit of detection using standard ELISA methods, down to a sub-picogram level. Moreover, the technique has been demonstrated to be reliable also for a typical case of clinical interest, namely for detecting biomarkers of AD through an immunoreaction protocol, with a linear behavior in the pg/mL range. In perspective, this p-jet technique can be exploited in a wide range of clinical cases where the clinician needs to determine the amount of low abundant biomarker molecules in peripheral human fluids to perform an early diagnosis, as in the case of AD biomarkers.

4.5 Surface tension measurements

The STs (γ) of the protein solutions (800 $\mu\text{g/ml}$, 400 $\mu\text{g/ml}$, and 40 $\mu\text{g/ml}$) were evaluated as described in Section 3.9. Figure 39 shows that A β 1-42 solutions 800 $\mu\text{g/ml}$ and 400 $\mu\text{g/ml}$ (day 0), had the typical sigmoidal trends common for proteins and emulsifiers⁹⁶. Specifically, two different regions, corresponding to unsaturated and saturated adsorption layers (plateau regions), were observed (see Figure 40). In fact, when an aqueous solution is in contact with an air phase, a finite time is required for the surface-active species to diffuse, adsorb at the interface, and reach the equilibrium value¹⁰¹. The equilibrium values (γ_{eq}) were determined from the plateau regions and were equal to $43 \pm 0.6 \text{ mNm}^{-1}$ for 800 $\mu\text{g/mL}$ and $44 \pm 0.8 \text{ mNm}^{-1}$ for 400 $\mu\text{g/mL}$. Whereas the initial surface tension (γ_0) values were $55 \pm 1 \text{ mNm}^{-1}$ for 800 $\mu\text{g/mL}$ and $61 \pm 0.4 \text{ mNm}^{-1}$ for 400 $\mu\text{g/mL}$. In the case of A β 1-42 at the concentration of 40 $\mu\text{g/ml}$, during the first 3 minutes, no surface tension decrease was observed, but the ST remained constant at a value of $71.3 \pm 0.2 \text{ mNm}^{-1}$. Besides, it took more than 40 minutes for equilibrium to be attained (see Figure 26). On the contrary, for higher concentrations (800 $\mu\text{g/mL}$, 400 $\mu\text{g/mL}$) the STs quickly decreased as observed for usual surfactants and proteins⁷⁸, and the equilibrium was reached in 20 minutes. The ST for the control solution (0 $\mu\text{g/mL}$) was $71 \pm 0.2 \text{ mNm}^{-1}$ and remained constant at this value for the 40 minutes considered, highlighting that the A β 1-42 was a surface-active species and, this determined the ST decrease. These first considerations were thoroughly investigated by using the mathematical models described in section 3.10.2, and by obtaining the graph reported in Figure 28.

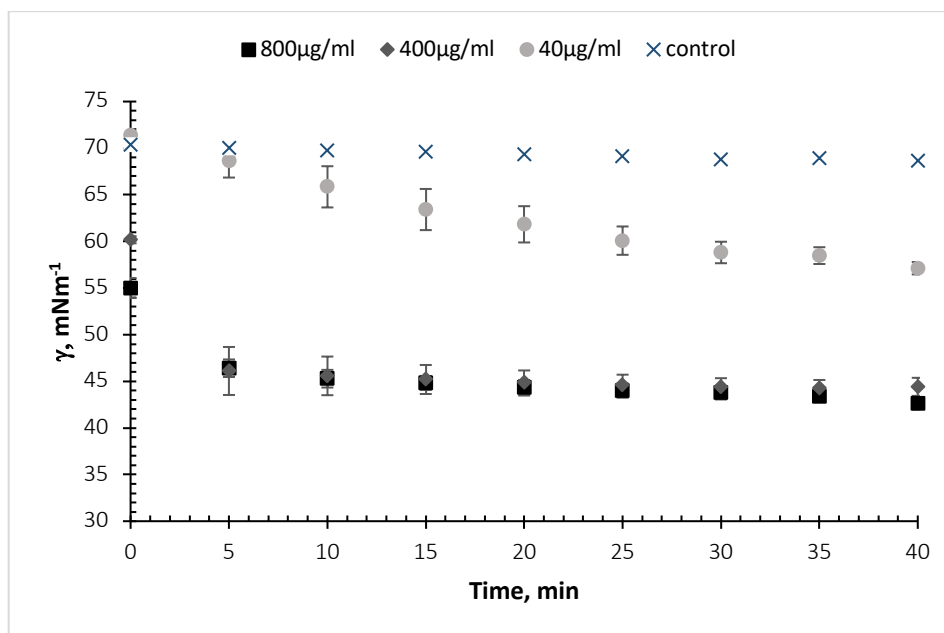


Figure 27. STs trends of Aβ1-42 solutions at 800 μg/mL (black square), 400 μg/mL (grey diamond), 40 μg/mL (light grey circle), 0 μg/mL (blue x).

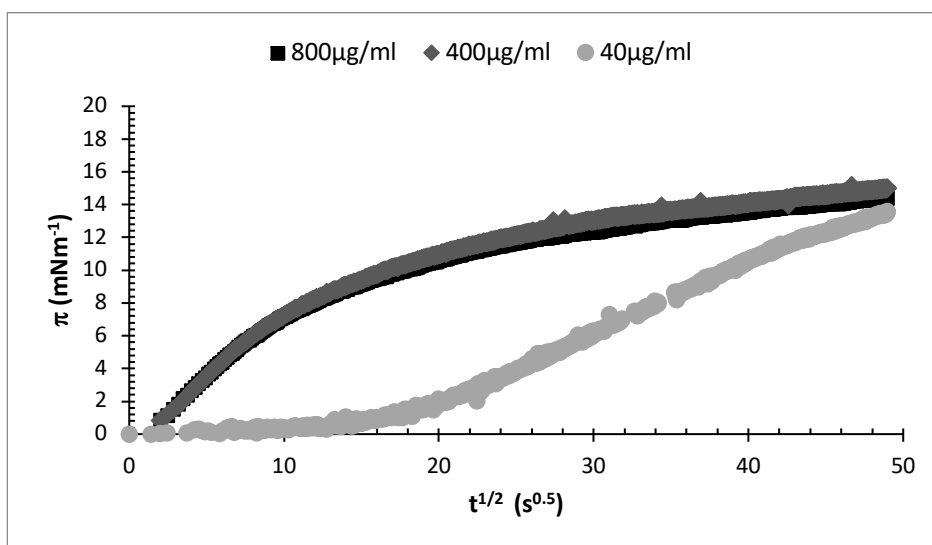
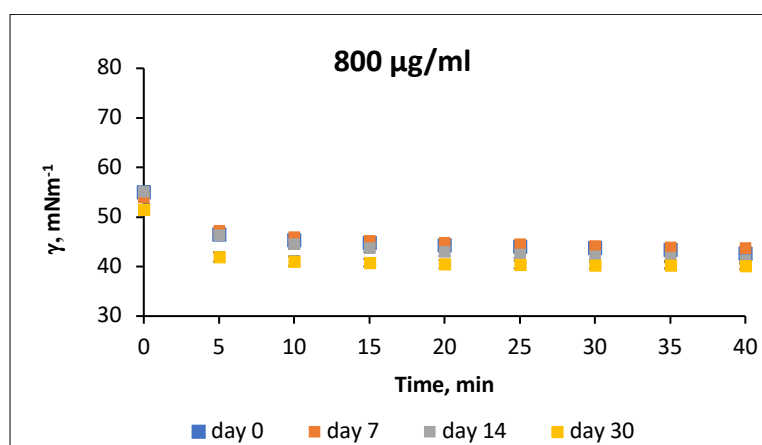


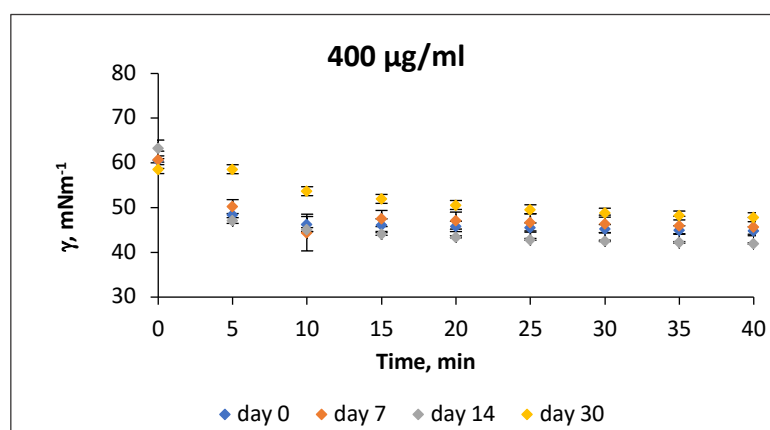
Figure 28. Temporal evolution of surface pressure, π , of Aβ1-42 at the air/water interface, at 800 μg/mL (black square), 400 μg/mL (grey diamond), 40 μg/mL (light grey circle). Data are reported as a function of time, t , square root according to Eq. (3). Error bars are not reported to make the figure more readable. The standard error was computed over three repetitions and is lower than 10%.

Data arranged according to equation (3) were reported in Figure 28, they have shown that at day 0, the lowest concentration (40 μg/mL) was characterized by an initial period where there was no change in the interfacial pressure (*lag* or *induction* period)^{68,74}. Conversely, for the highest concentrations, the interfacial pressure immediately changed. These results agreed with the literature data for proteins, it is well-known that the induction period shortens as protein concentration is increased^{79,80}. In fact, for the highest concentrations, no lag period was observed but the induction time was found to decrease as the bulk concentration was increased. The induction is caused by two factors: first, proteins may have a critical surface concentration only above which they can engage in

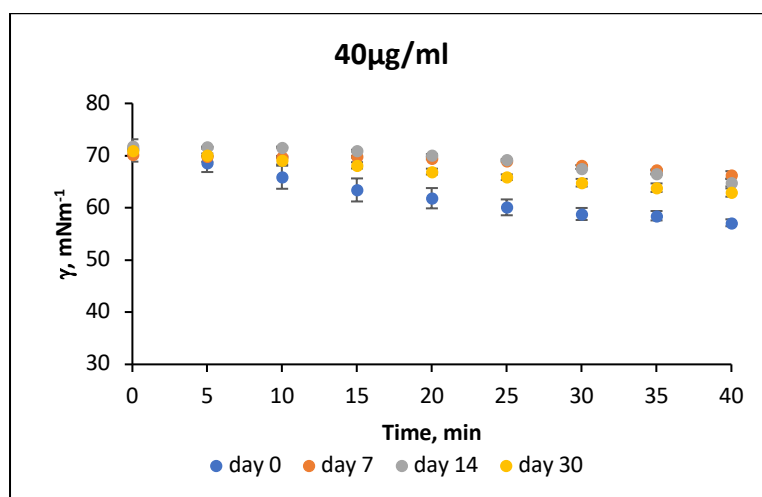
intermolecular cohesive interactions at the interface and cause a greater reduction in surface tension. Second, it might be related to the time needed for the adsorbed proteins to unfold at the interface and to initiate cohesive interactions^{78–84}. In this second case, the induction period is dependent on the protein stability⁸⁵. Since the 40 $\mu\text{g/mL}$ was quite diluted, the induction period (143 seconds, as reported in Table 6) at day 0 could be related to the insufficient adsorption of A β 1-42 to the interface. In other words, the amount of adsorbed proteins was not enough, thus, the interactions between them were not appreciable and the ST did not change. Even though on day 0 for the higher concentrations (800 and 400 $\mu\text{g/mL}$), there was no induction period (see Figure 28), it was noteworthy to notice that on day 30, the lag period arose for the concentration of 400 $\mu\text{g/mL}$ and it increased for the 40 $\mu\text{g/mL}$ (see Figure 29b and Table 8). This was an outstanding result, suggesting that the protein stability was changing over time.



(a)



(b)



(c)

Figure 29. STs trends of Aβ1-42 (a) 800 μg/ml at day 0 (blue square), day 7 (orange square), day 14 (grey square), day 30 (yellow square), (b) 400 μg/ml at day 0 (blue diamond), day 7 (orange diamond), day 14 (grey diamond), day 30 (yellow diamond), (c) 40 μg/ml at day 0 (blue circle), day 7 (orange circle), day 14 (grey circle), day 30 (yellow circle).

Additionally, the kinetic constants (K_d , K_{ads} , and K_r) and the lag times were extrapolated as described in section 3.10.2 and were summarized in Table 6. From day 0 to day 30, in the case of 800 μg/ml, the results of the ANOVA test ($Pr>F=8\%$) suggested that K_d did not significantly vary as well as the K_{ads} . This evidence can be attributed to the fact that 800 μg/ml was a concentration very high, so, the solution was extremely crowded in proteins, and these were so close to each other to constrain their diffusion and adsorption at the interface. As a result, the processes (diffusion, adsorption) were extremely slow, and the corresponding kinetics did not remarkably change over time. Conversely, for the lower concentration (40 μg/ml), the K_d decreased significantly over time ($Pr>F=0.3\%$). Moreover, the Dunn test highlighted that there was a significant difference in the K_d between day 0 and day 30 ($Pr>Diff=0.001$). The same result was obtained in the case of 400 μg/ml, the K_d remarkably decreased from day 0 to day 30 ($Pr>Diff=0.001$). These results suggested that the protein on day 30 was diffusing slower than on day 0, probably due to its agglomeration. In fact, as the number of proteins as single entities in the volume solution decreased, the number of agglomerates increased, and these agglomerates diffused slower. In fact, the agglomerates were bigger than the single proteins and their diffusion was hindered. Besides, for 40 μg/ml the K_{ads} did not change over time ($Pr>F=6\%$). The solution of 40 μg/ml was too diluted; thus, the adsorbed proteins were not so many to see variations in terms of adsorption during the time. Whereas, for 400 μg/ml the proteins adsorbed at the interface were sufficient to verify that K_{ads} changed over time ($Pr>F=0.01\%$). Specifically, there was a decrease between day 0 and day 30 ($Pr>Diff=0.01\%$). Since there were fewer proteins that could diffuse due to the presence of agglomerates, clearly, fewer of them were adsorbed at the interface, so K_{ads} decreased. Even though the proteins adsorbed at the interface in the case of 40 μg/ml were not sufficient to evaluate a K_{ads} variation over time, one can see in Table 6 that K_{ads} for the 40 μg/ml was higher than K_{ads} for the 400 and 800 μg/ml. This result was attributed to the adsorption process at the interface. In fact, proteins for adsorbing at the interface must expose

their hydrophobic part to the interface and their hydrophilic part to the bulk, this structural disposition needs time. This time decreases as the protein concentration decreases. In fact, proteins in diluted conditions can easier move and find the right disposition at the interface, thus they are faster adsorbed. On the contrary, when the concentration was higher the interface was protein crowded and it was hard to move and find the right position, hence, to adsorb at the interface.

	40µg/ml				400µg/ml				800µg/ml			
	t _{lag} s	K _d mNm ⁻¹ s ^{-0.5}	K _{ads} 10 ⁻³ , s ⁻¹	K _r 10 ⁻³ , s ⁻¹	t _{lag} s	K _d mNm ⁻¹ s ^{-0.5}	K _{ads} 10 ⁻³ , s ⁻¹	K _r 10 ⁻³ , s ⁻¹	t _{lag} s	K _d mNm ⁻¹ s ^{-0.5}	K _{ads} 10 ⁻³ , s ⁻¹	K _r 10 ⁻³ , s ⁻¹
day 0	143	0.4	3	/	/	1.5	1.3	3.5	/	0.8	1.1	/
day 7	498	0.1	5	/	/	0.8	1.2	2.9	/	0.5	1.2	/
day 14	400	0.1	0.7	/	2	1.4	1.5	4.0	/	0.6	1.3	/
day 30	400	0.1	0.6	/	3.82	0.4	0.5	1.0	/	0.7	1.5	/

Table 8. Velocity of diffusion (K_d), adsorption (K_{ads}) and rearrangement (K_r) for Aβ1-42 solutions at 40 µg/ml, 400 µg/ml and 800 µg/ml, evaluated at day 0, day 7, day 14 and day 40.

Concerning the rearrangement step, for 800 µg/ml was not found (see Table 6) since the proteins were so many and so crowded that they cannot do any movement/rearrangement at the interface. For 40 µg/ml the solution was too diluted that more time would have been needed to see the rearrangement. On the other hand, in the case of 400 µg/ml was possible to evaluate a rearrangement step (see Table 6). Since the Critical Micellar Concentration (CMC) was reached at 400 µg/ml (see Figure 30), this was the optimal condition to have protein movement on the interface.

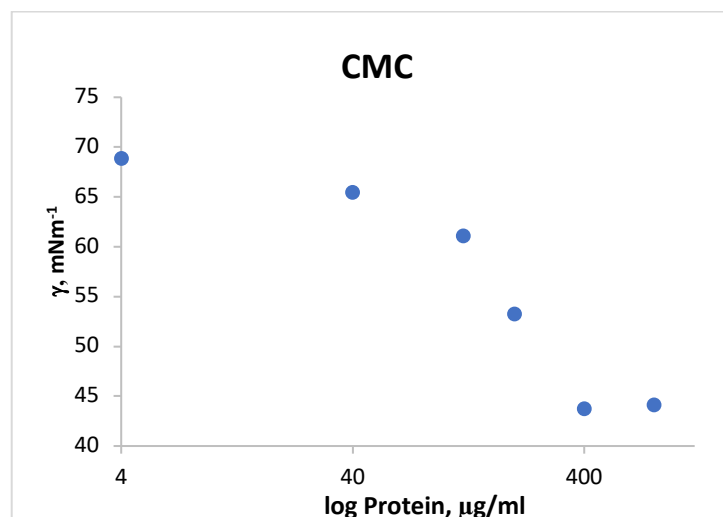


Figure 30. CMC evaluation, the concentration tested were: (0.4, 4, 40, 120, 200, 400, 800)mg/ml.

4.6 Fluorescence intensity measurements

To verify the hypothesis about the influence of protein agglomeration on the sensitivity of an AD diagnostic test, an immunoreaction protocol was carried out, so the FIs were evaluated. The results showed that at day 0 the FIs were equal to $(6.21 \pm 0.64)E+07$ a.u. for 800 µg/ml and 400 µg/ml and to $(3.59 \pm 0.68)E+07$ a.u. for 40 µg/ml. In the case of 40 µg/ml, there was no significant difference

between groups ($Pr>F=6\%$). This result could be explained considering that the immunoreaction protocol was realized by depositing the protein with a traditional pipette, this method was constrained by the diffusion effects of the molecules on the reaction slide, which drastically reduced the LOD. For instance, the lack of manual deposition of biomolecules was thoroughly described in our previous papers^{61–63,68}. As a result, for the lower concentration, the sensitivity was not sufficient to detect a change in terms of FI. Whereas for 400 $\mu\text{g/ml}$ and 800 $\mu\text{g/ml}$ significant differences ($Pr>F=0.01\%$) were found over time. Specifically, it was proved that the FI on day 30 was significantly different from the FI on day 0 ($Pr>\text{Diff}=0.01\%$). In fact, as shown in Figure 31 the FIs drastically decreased on day 30, for 800 $\mu\text{g/ml}$ and 400 $\mu\text{g/ml}$.

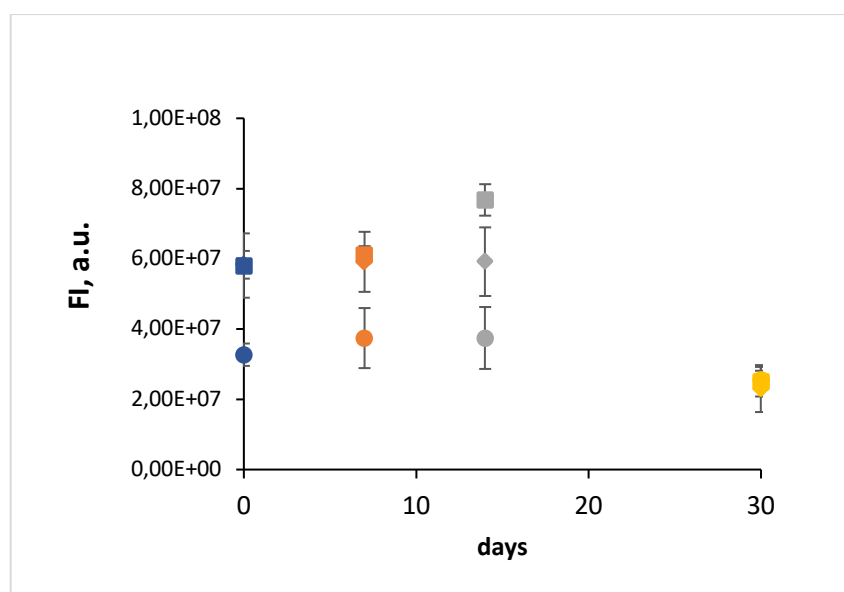


Figure 31. FIs trends of A β 1-42 at concentration of 800 $\mu\text{g/ml}$ at day 0 (blue square), day 7 (orange square), day 14 (grey square), day 30 (yellow square), of 400 $\mu\text{g/ml}$ at day 0 (blue diamond), day 7 (orange diamond), day 14 (grey diamond), day 30 (yellow diamond), of 40 $\mu\text{g/ml}$ at day 0 (blue circle), day 7 (orange circle), day 14 (grey circle), day 30 (yellow circle).

Chapter 5 Conclusions

In this thesis work, developed in the framework of the European project “SensApp”, it was proposed an innovative approach to detect low abundant AD biomarkers as a potential device that in perspective could be introduced in the clinical diagnosis, in all of those cases where highly diluted biomarkers have to be detected. Firstly, the thesis focused the attention on a deep study of the standard methods applied in the clinical routine, to understand their approach and limits. The AD standard methods of diagnosis include invasive procedures applied only when the symptoms are clearly exposed, and it just needs a confirmation of the presence of the pathological brain process, as well as PER, MRI or lumbar puncture. To dosage the biomarkers in the cerebrospinal fluid it is adopted the lumbar puncture procedure, which allows one the collection of a sufficient volume to apply the ELISA test, this test takes advantage of the bond biomarker-antibody to quantify the concentration of the analytes. The lumbar puncture has high invasiveness, for this reason, the diagnosis is often postponed over time, leading to a late diagnosis. On the other hand, some studies propose alternative ways to detect the biomarkers in the plasma fluid. The huge limits of these are the limit of detection, over the pg/ml. To overcome the ELISA LOD on the plasma fluid, we developed an innovative technology “drop-split-and-stack” (DSS) that allows the concentration of micro-droplets of the biological sample containing the biomarkers of interest on a very limited area of a support dedicated. In other words, our approach was designed as a biosensor able to reduce diffusion phenomena of the biomolecules of interest, maximising the concentration of biomolecules, in this way it could be obtained a sensitivity under the pg/ml. It exploits the pyroelectric effect in lithium niobate crystals. The pyroelectric crystal, functionalized with a thermal source, acts as a source of the pyro-electro-hydrodynamic jet, which activates the rapid split of tiny droplets ("split") on the same site ("μ-site") on the reaction support. The μ-droplets of fluid containing the biomarkers are concentrated on a definite area of the slide support, so we have a higher signal of biomarkers in a restricted area. This allows us to overcome the LOD under the pg/ml and open the route to an early diagnosis using the plasma fluid. These biomolecules collected at very low concentrations, with this approach had to be quantifiable and labelled. Thus, starting from the literature data, it was developed an immunoreaction protocol that improves and overcomes the limit of the standard immunoreaction protocol, we performed an *ELISA-like*. It was tested different process conditions and identified the parameters that allow the production of a quantifiable and reproducible result.

Furthermore, here it was performed a non-destructive method to investigate protein aggregation. Considering the nature of the AD biomarkers to aggregate, it could be very interesting to examine the stability of their conformations. In fact, the most popular approach includes the loss of the sample after the measurements, our technique offered a solution to this inconvenience. It used the surface tension analysis associated with the mathematic models to understand protein folding. The change of structure conformation modulates the migration and the adsorption of the biomolecules from the

bulk to the interface. At the end of this process, it was obtained a different surface tension that showed the degree of protein aggregation.

The initial phase of the project was focused on the choice of biomarkers and the preliminary tests. The first AD biomarker tested was Amyloid β 1-40. Its stability preserved us from the protein aggregates that could have undermined our reaction regardless of the other variables applied. With this approach, changing step by step every component of the protocol reaction, it was demonstrated the reliability of the method. Moreover, with the preliminary tests, it was evaluated the choice of the different slides as reaction support, the opportunities of mixing the protein sample with other solutions to improve the repeatability of the spots, or a pre-treatment of the slide used during the immunoreaction, to increase signal strength and reduce background noise. At the same time, different experiments were performed to assess the incubation of the various reaction solutions, to improve the signal obtained at the lowest concentration. The preliminary analysis led at the conclusion:

- avoiding the mix of the protein solution with buffer solutions of different chemical nature, the proteins in the solution were more stable
- using the reaction support functionalized with NH_3^+ ammino groups, it was guaranteed a stable bond with the biomarkers
- activating the reaction support before the spotting of the protein solution there were a worst diffusion mechanism

Starting from these preliminary tests, it was thorough and characterized the p-jet set-up, comparing it to a commercial biospotter. Our p-jet sensor showed the ability to enhance the fluorescence signal of low abundant biomolecules linearly by increasing the number of accumulated jets. This technique provided an easy-to-use procedure that can tune the accumulation rate of target molecules in highly diluted solutions. The reliability of the technique has been demonstrated by the linear behaviour of the fluorescence signal as a function of the probe concentration. The results of the useful comparative study demonstrated the ability of the p-jet sensor to push the sensitivity down to the sub-picogram level against the microgram level achieved in the case of the biospotter. The p-jet sensor was proven to have a LOD at 0.01 pg/ml. Moreover, the technique was demonstrated to be reliable also for a typical case of clinical interest, namely for detecting biomarkers of AD through an immunoreaction protocol, with a linear behaviour in the pg/mL range and a LOD of 4 pg/ml. This is a very promising result since the typical limit of detection reported for this kind of biomarker through well-established ELISA kits available in the market is around 50 pg/ml^{102,103}.

For these reasons, in future the p-jet will be tested in a wide range of clinical cases where the clinician needs to determine the amount of low abundant biomarker molecules in peripheral human fluids to perform an early diagnosis, as in the case of AD biomarkers. Moreover, this approach could open the route not only to severe pathological conditions but also to the monitoring of human health. In fact, great interest is aroused in biosensors set up in fields such as space medicine. They could be useful to evaluate the astronauts' health during the mission, which compromises human physiological

homeostasis. Nowadays, many assays are proposed to measure biomolecules, and the biosensor approach emerges as one of the most promising platforms for this purpose. This approach, with its proven super-sensitivity, offers a solution to all the conditions where it is crucial to understand the minimal variation of the biochemical or pathological mechanisms.

Furthermore, interesting results were obtained in the analysis of the protein aggregation correlated to the surface tension and the fluorescence signal. It is known that the fluorescence signal is correlated to the aggregation of proteins. In fact, the protein misfolding hides the active binding site that allows the antibody to recognize its specific biomolecules. Without bond biomarker-antibody, it is impossible to demonstrate and quantify the concentration of analytes in the solution. In the case of the concentration of 800 $\mu\text{g/ml}$ and 400 $\mu\text{g/ml}$, it was found a reduction in fluorescence signal during the time, emphasizing how much important is protein stability in the immunoreaction protocol. At the lowest concentration, 40 $\mu\text{g/ml}$, it did not quantifiable considering the instrument's sensitivity. Moreover, about the quantification of the aggregation, at the concentration of 400 $\mu\text{g/ml}$ and 40 $\mu\text{g/ml}$, it was measured the agglomeration state of the proteins. Whereas the biomolecules at 800 $\mu\text{g/ml}$ did not confirm the trend because of their higher concentration, which limited the biomolecules' diffusion and adsorption at the interface, probably due to the migration time extended beyond the analysis time. In conclusion, with the promising results obtained, this approach can be considered an innovative and prospective method to evaluate the aggregation of the AD biomarkers but also of the disease that are caused by a pathological protein aggregation.

References

1. Nakamura, A. *et al.* High performance plasma amyloid- β biomarkers for Alzheimer's disease. *Nature* **554**, 249–254 (2018).
2. <https://www.who.int/news-room/fact-sheets/detail/dementia>. [https1.pdf](#).
3. Uddin, M. S. & Kabir, M. T. Emerging signal regulating potential of genistein against Alzheimer's disease: A promising molecule of interest. *Front. Cell Dev. Biol.* **7**, 1–12 (2019).
4. Terry, R. D. Alzheimer's Disease at mid-Century (1927–1977) and a little more. *Alzheimer 100 Years Beyond* 59–61 (2006) doi:10.1007/978-3-540-37652-1_5.
5. Blennow, K., de Leon, M. J. & Zetterberg, H. Alzheimer's disease. *Lancet* **368**, 387–403 (2006).
6. Ekman, U., Ferreira, D. & Westman, E. The A/T/N biomarker scheme and patterns of brain atrophy assessed in mild cognitive impairment. *Sci. Rep.* **8**, 1–10 (2018).
7. Dixon, R. M., Bradley, K. M., Budge, M. M., Styles, P. & Smith, A. D. Longitudinal quantitative proton magnetic resonance spectroscopy of the hippocampus in Alzheimer's disease. *Brain* **125**, 2332–2341 (2002).
8. Bozzali, M., Padovani, A., Caltagirone, C. & Borroni, B. Regional Grey Matter Loss and Brain Disconnection Across Alzheimer Disease Evolution. *Curr. Med. Chem.* **18**, 2452–2458 (2011).
9. MD, D. W. D. the Pathogenesis of senile plasques. *J. neuropathology Exp. Neurol.* **56**, 321–339 (1997).
10. Hardy J A, H. G. A. Alzheimer's disease: the amyloid cascade hypothesis. *Sciences (New York)*. **5**, 184 (1992).
11. Jan, A., Gokce, O., Luthi-Carter, R. & Lashuel, H. A. The ratio of monomeric to aggregated forms of A β 40 and A β 42 is an important determinant of amyloid- β aggregation, fibrillogenesis, and toxicity. *J. Biol. Chem.* **283**, 28176–28189 (2008).
12. Zhou, Z. D. *et al.* The roles of amyloid precursor protein (APP) in neurogenesis, implications to pathogenesis and therapy of alzheimer Disease (AD). *Cell Adhes. Migr.* **5**, (2011).
13. Galozzi, S., Marcus, K. & Barkovits, K. Amyloid- β as a biomarker for Alzheimer's disease: Quantification methods in body fluids. *Expert Rev. Proteomics* **12**, 343–354 (2015).
14. <https://www.uniprot.org/uniprotkb/P05067/entry#structure>. [app protein.pdf](#).
15. Hardy, J. & Selkoe, D. J. The amyloid hypothesis of Alzheimer's disease: Progress and problems on the road to therapeutics. *Science (80-.)*. **297**, 353–356 (2002).
16. Pike, C. J., Walencewicz, A. J., Glabe, C. G. & Cotman, C. W. In vitro aging of β -amyloid protein causes peptide aggregation and neurotoxicity. *Brain Res.* **563**, 311–314 (1991).
17. Strozzyk, D., Blennow, K., White, L. R. & Launer, L. J. CSF A β 42 levels correlate with amyloid-neuropathology in a population-based autopsy study. *Neurology* **60**, 652–656 (2003).
18. De Simone, A. *et al.* Intrinsic disorder modulates protein self-assembly and aggregation. *Proc. Natl. Acad. Sci. U. S. A.* **109**, 6951–6956 (2012).
19. Bianco, V., Franzese, G. & Coluzza, I. In Silico Evidence That Protein Unfolding is a Precursor of Protein Aggregation. *ChemPhysChem* **21**, 377–384 (2020).
20. Uversky, V. N. & Fink, A. L. Conformational constraints for amyloid fibrillation: The importance of being unfolded. *Biochim. Biophys. Acta - Proteins Proteomics* **1698**, 131–153

- (2004).
21. Christopher M. Dobson. Protein misfolding , evolution and disease. *Trends Biochem. Sci.* **24**, 329–332 (1999).
 22. Uversky, V. Amyloidogenesis of Natively Unfolded Proteins. *Curr. Alzheimer Res.* **5**, 260–287 (2008).
 23. Lansbury, J. Evolution of amyloid: What normal protein folding may tell us about fibrillogenesis and disease. *Proc. Natl. Acad. Sci. U. S. A.* **96**, 3342–3344 (1999).
 24. Renvoize, E., Hanson, M. & Dale, M. Prevalence and causes of young onset dementia in an English health district. *Int. J. Geriatr. Psychiatry* **26**, 106–107 (2011).
 25. Mendez, M. F. Early-onset Alzheimer disease and its variants. *Contin. Lifelong Learn. Neurol.* **25**, 34–51 (2019).
 26. Coon, D. W., Davies, H., McKibben, C. & Gallagher-Thompson, D. The psychological impact of genetic testing for Alzheimer disease. *Genet. Test.* **3**, 121–131 (1999).
 27. Koedam, E. L. G. E. *et al.* Early-onset dementia is associated with higher mortality. *Dement. Geriatr. Cogn. Disord.* **26**, 147–152 (2008).
 28. Panegyres, P. K. & Chen, H. Y. Differences between early and late onset Alzheimer’s disease. *Am. J. Neurodegener. Dis.* **2**, 300–306 (2013).
 29. Winblad, B. *et al.* Mild cognitive impairment - Beyond controversies, towards a consensus: Report of the International Working Group on Mild Cognitive Impairment. *J. Intern. Med.* **256**, 240–246 (2004).
 30. Li, X. L., Hu, N., Tan, M. S., Yu, J. T. & Tan, L. Behavioral and Psychological Symptoms in Alzheimer’s Disease. *Biomed Res. Int.* **2014**, (2014).
 31. Lyketsos, C. G. *et al.* Neuropsychiatric symptoms in Alzheimer’s disease. *Alzheimer’s Dement.* **7**, 532–539 (2011).
 32. Gauthier, S. & Scheltens, P. Can we do better in developing new drugs for Alzheimer ’ s disease ? *Alzheimer’s Dement.* **5**, 489–491 (2010).
 33. Tanvir Kabir, M. *et al.* Combination drug therapy for the management of alzheimer’s disease. *Int. J. Mol. Sci.* **21**, (2020).
 34. Deardorff, W. J. & Grossberg, G. T. A fixed-dose combination of memantine extended-release and donepezil in the treatment of moderate-to-severe Alzheimer’s disease. *Drug Des. Devel. Ther.* **10**, 3267–3279 (2016).
 35. Cummings, J. *et al.* Drug development in Alzheimer’s disease: The path to 2025. *Alzheimer’s Res. Ther.* **8**, 1–12 (2016).
 36. Bateman, R. J. *et al.* Clinical and Biomarker Changes in Dominantly Inherited Alzheimer’s Disease. *N. Engl. J. Med.* **367**, 795–804 (2012).
 37. Pietrzak, K. & Czarnecka, K. New Perspectives of Alzheimer Disease Diagnosis – the Most Popular and Future Methods. 34–43 (2018) doi:10.2174/1573406413666171002120847.
 38. Liu, S. *et al.* EARLY DIAGNOSIS OF ALZHEIMER ’ S D ISEASE WITH DEEP LEARNING. *2014 IEEE 11th Int. Symp. Biomed. Imaging* 1015–1018 (2014) doi:10.1109/ISBI.2014.6868045.
 39. Agnello, L. *et al.* Diagnostic accuracy of cerebrospinal fluid biomarkers measured by chemiluminescent enzyme immunoassay for Alzheimer disease diagnosis. *Scand. J. Clin. Lab. Invest.* **80**, 313–317 (2020).
 40. Bittner, T. *et al.* Technical performance of a novel, fully automated electrochemiluminescence immunoassay for the quantitation of β -amyloid (1-42) in human cerebrospinal fluid. *Alzheimer’s Dement.* **12**, 517–526 (2016).

41. <https://www.fujirebio.com/en/products-solutions/innotest-beta-amyloid142-RUO>.
42. Liu, Y., Qing, H. & Deng, Y. Biomarkers in Alzheimer's disease analysis by mass spectrometry-based proteomics. *Int. J. Mol. Sci.* **15**, 7865–7882 (2014).
43. Gershoni, J. M., Roitburd-Berman, A., Siman-Tov, D. D., Tarnovitski Freund, N. & Weiss, Y. Epitope Mapping. *BioDrugs* **21**, 145–156 (2007).
44. Ismail, A. A. A., Walker, P. L., Cawood, M. L. & Barth, J. H. Interference in immunoassay is an underestimated problem. *Ann. Clin. Biochem.* **39**, 366–373 (2002).
45. Wang, Z. *et al.* Development of an antigen capture enzyme-linked immunosorbent assay for virus detection based on porcine epidemic diarrhea virus monoclonal antibodies. *Viral Immunol.* **28**, 184–189 (2015).
46. Li, D. & Mielke, M. M. An Update on Blood-Based Markers of Alzheimer's Disease Using the SiMoA Platform. *Neurol. Ther.* **8**, 73–82 (2019).
47. Metkar, S. K. & Girigoswami, K. Diagnostic biosensors in medicine – A review. *Biocatal. Agric. Biotechnol.* **17**, 271–283 (2019).
48. Sassolas, A., Blum, L. J. & Leca-Bouvier, B. D. Immobilization strategies to develop enzymatic biosensors. *Biotechnol. Adv.* **30**, 489–511 (2012).
49. Vestergaard, M., Kerman, K. & Tamiya, E. An overview of label-free electrochemical protein sensors. *Sensors* **7**, 3442–3458 (2007).
50. Piriya V.S, A. *et al.* Colorimetric sensors for rapid detection of various analytes. *Mater. Sci. Eng. C* **78**, 1231–1245 (2017).
51. Mehrotra, P. Biosensors and their applications - A review. *J. Oral Biol. Craniofacial Res.* **6**, 153–159 (2016).
52. Wang, J. Electrochemical glucose biosensors. *Chem. Rev.* **108**, 814–825 (2008).
53. Li, C. *et al.* Improvement of enzyme-linked immunosorbent assay for the multicolor detection of biomarkers. *Chem. Sci.* **7**, 3011–3016 (2016).
54. Cruz, H. J., Rosa, C. C. & Oliva, A. G. Immunosensors for diagnostic applications. *Parasitol. Res.* **88**, 4–7 (2002).
55. Cesewski, E. & Johnson, B. N. Electrochemical biosensors for pathogen detection. *Biosens. Bioelectron.* **159**, 112214 (2020).
56. Choi, M. M. F. Progress in enzyme-based biosensors using optical transducers. *Microchim. Acta* **148**, 107–132 (2004).
57. Urban Ekman, D. F. & E. W. The A/T/N biomarker scheme and patterns of brain atrophy assessed in mild cognitive impairment. *Nat. Sci. reports* **06**, (2018).
58. Gong, P. & Grainger, D. W. Comparison of DNA immobilization efficiency on new and regenerated commercial amine-reactive polymer microarray surfaces. *Surf. Sci.* **570**, 67–77 (2004).
59. Gil Rosa, B. *et al.* Multiplexed immunosensors for point-of-care diagnostic applications. *Biosens. Bioelectron.* **203**, 114050 (2022).
60. Lang, S. B. Pyroelectricity: From ancient curiosity to modern imaging tool. *Phys. Today* **58**, 31–36 (2005).
61. R. Rega, J. F. Muñoz Martinez, M. Mugnano, E. Oleandro, O. Gennari, P. Orlando, G. Cabassi, V. Pelizzola,, P. Ferraro, S. G. A pyroelectric-based system for sensing low abundant lactose molecules. *Proc. Opt. Methods Insp. Charact. Imaging Biomater. IV*; **Volume 110**,.
62. Grilli, S. *et al.* Active accumulation of very diluted biomolecules by nano-dispensing for

- easy detection below the femtomolar range. *Nat. Commun.* **5**, 1–6 (2014).
63. Rega, R. *et al.* Detecting collagen molecules at picogram level through electric field-induced accumulation. *Sensors (Switzerland)* **20**, 1–11 (2020).
 64. Gennari, O. *et al.* Investigation on cone jetting regimes of liquid droplets subjected to pyroelectric fields induced by laser blasts. *Appl. Phys. Lett.* **106**, (2015).
 65. Melcher, J. R. & Taylor, G. I. Electrohydrodynamics: A Review of the Role of Interfacial Shear Stresses. *Annu. Rev. Fluid Mech.* **1**, 111–146 (1969).
 66. Taylor, G. & A, P. R. S. L. Disintegration of water drops in an electric field. *Proc. R. Soc. London. Ser. A. Math. Phys. Sci.* **280**, 383–397 (1964).
 67. Ferraro, P., Coppola, S., Grilli, S., Paturzo, M. & Vespini, V. Dispensing nano-pico droplets and liquid patterning by pyroelectrodynamic shooting. *Nat. Nanotechnol.* **5**, 429–435 (2010).
 68. REGA, R. *et al.* Highly sensitive detection of low abundant molecules by pyro-electrohydro-dynamic jetting. **11361**, 38 (2020).
 69. Rega, R. *et al.* SensApp: a FET-open project for developing a supersensor able to detect Alzheimer's disease biomarkers in blood. 58 (2021) doi:10.1117/12.2596966.
 70. Li, Y. & Yu, S. M. Targeting and mimicking collagens via triple helical peptide assembly. *Curr. Opin. Chem. Biol.* **17**, 968–975 (2013).
 71. Hadler-Olsen, E., Fadnes, B., Sylte, I., Uhlin-Hansen, L. & Winberg, J. O. Regulation of matrix metalloproteinase activity in health and disease. *FEBS J.* **278**, 28–45 (2011).
 72. K. Okuyama, Revisiting the molecular structure of collagen, *Connect. Tissue Res.* **49** (2008) 299–310. **49**, 2008 (2008).
 73. Surazynski, A., Milytyk, W., Palka, J. & Phang, J. M. Prolidase-dependent regulation of collagen biosynthesis. *Amino Acids* **35**, 731–738 (2008).
 74. Osmekhina, E., Neubauer, A., Klinzing, K., Myllyharju, J. & Neubauer, P. Sandwich ELISA for quantitative detection of human collagen prolyl 4-hydroxylase. *Microb. Cell Fact.* **9**, 1–11 (2010).
 75. Leeming, D. J. *et al.* Serological investigation of the collagen degradation profile of patients with chronic obstructive pulmonary disease or idiopathic pulmonary fibrosis. *Biomark. Insights* **7**, 119–126 (2012).
 76. Abcam. Human Pro-Collagen I alpha 1 CatchPoint ® Kit. **05**, 6220 (2018).
 77. Willumsen, N. *et al.* Serum biomarkers reflecting specific tumor tissue remodeling processes are valuable diagnostic tools for lung cancer. *Cancer Med.* **3**, 1136–1145 (2014).
 78. Safdar, Z. *et al.* Circulating Collagen Biomarkers as Indicators of Disease Severity in Pulmonary Arterial Hypertension. *JACC Hear. Fail.* **2**, 412–421 (2014).
 79. Sorensen, A. G. *et al.* A 'vascular normalization index' as potential mechanistic biomarker to predict survival after a single dose of cediranib in recurrent glioblastoma patients. *Cancer Res.* **69**, 5296–5300 (2009).
 80. Wolf, K. J., Chen, J., Coombes, J. D., Aghi, M. K. & Kumar, S. Dissecting and rebuilding the glioblastoma microenvironment with engineered materials. *Nat. Rev. Mater.* (2019) doi:10.1038/s41578-019-0135-y.
 81. Bio-labs, G. & Bio-labs, G. ONCYTE ® Guide to Protein Microarrays. 1–24 (2011).
 82. arrayit.pdf.
 83. KERWIN, B. A. Polysorbates 20 and 80 Used in the Formulation of Protein Biotherapeutics: Structure and Degradation Pathways. *J. Pharm. Sci.* **97**, 2924–2935 (2008).

84. Lee, J., Purushothaman, B. & Song, J. M. Inkjet Bioprinting on Parchment Paper for Hit Identification from Small Molecule Libraries. *ACS Omega* **5**, 588–596 (2020).
85. Al-Shibaany, Z. Y. A., Hedley, J., Huo, D. & Hu, Z. Micromachining lithium niobate for rapid prototyping of resonant biosensors. *IOP Conf. Ser. Mater. Sci. Eng.* **65**, (2014).
86. Al-Shibaany, Z. Y. A., Penchev, P., Hedley, J. & Dimov, S. Laser micromachining of Lithium niobate-based resonant sensors towards medical devices applications. *Sensors (Switzerland)* **20**, (2020).
87. Woodward, R. P. Surface Tension Measurements Using the Drop Shape Method. *First Ten Angstroms Inc Tech. Inf.* 1–6 (2008).
88. Liu, H. & Cao, G. Effectiveness of the Young-Laplace equation at nanoscale. *Sci. Rep.* **6**, 1–10 (2016).
89. Adamson, A. & Gast, A. Arthur W. Adamson, Alice P. Gast - Physical chemistry of surfaces-Wiley (1997).pdf. (1997).
90. Farooq, U., Simon, S., Tweheyo, M. T., Øye, G. & Sjöblom, J. Interfacial Tension Measurements Between Oil Fractions of a Crude Oil and Aqueous Solutions with Different Ionic Composition and pH. *J. Dispers. Sci. Technol.* **34**, 701–708 (2013).
91. Vargaftik, N. B., Volkov, B. N. & Voljak, L. D. International Tables of the Surface Tension of Water. *J. Phys. Chem. Ref. Data* **12**, 817–820 (1983).
92. Camino, N. A., Pérez, O. E., Sanchez, C. C., Rodriguez Patino, J. M. & Pilosof, A. M. R. Hydroxypropylmethylcellulose surface activity at equilibrium and adsorption dynamics at the air-water and oil-water interfaces. *Food Hydrocoll.* **23**, 2359–2368 (2009).
93. Baldino, N., Angelico, R., Caputo, P., Gabriele, D. & Rossi, C. O. Effect of high water salinity on the adhesion properties of model bitumen modified with a smart additive. *Constr. Build. Mater.* **225**, 642–648 (2019).
94. Pérez, O. E., Sánchez, C. C., Pilosof, A. M. R. & Rodríguez Patino, J. M. Dynamics of adsorption of hydroxypropyl methylcellulose at the air-water interface. *Food Hydrocoll.* **22**, 387–402 (2008).
95. Baldino, N., Mileti, O., Lupi, F. R. & Gabriele, D. Rheological surface properties of commercial citrus pectins at different pH and concentration. *Lwt* **93**, 124–130 (2018).
96. Seta, L., Baldino, N., Gabriele, D., Lupi, F. R. & De Cindio, B. The effect of surfactant type on the rheology of ovalbumin layers at the air/water and oil/water interfaces. *Food Hydrocoll.* **29**, 247–257 (2012).
97. Pilosof, Rosa Baeza and Ana M. R., C. C. S. and J. M. R. P. Adsorption and Rheological properties of Biopolymers at the Air-Water Interface. *AIChE J.* **59**, 215–228 (2006).
98. Ward, A. F. H. & Tordai, L. Time-dependence of boundary tensions of solutions I. The role of diffusion in time-effects. *J. Chem. Phys.* **14**, 453–461 (1946).
99. Graham, D. E. & Phillips, M. C. Proteins at liquid interfaces. III. Molecular structures of adsorbed films. *J. Colloid Interface Sci.* **70**, 427–439 (1979).
100. George, R. A., Woolley, J. P. & Spellman, P. T. Ceramic capillaries for use in microarray fabrication. *Genome Res.* **11**, 1780–1783 (2001).
101. Keleşoğlu, S., Meakin, P. & Sjöblom, J. Effect of aqueous phase pH on the dynamic interfacial tension of acidic crude oils and myristic acid in Dodecane. *J. Dispers. Sci. Technol.* **32**, 1682–1691 (2011).
102. Vanderstichele, H. *et al.* Standardization of measurement of beta-amyloid (1-42) in cerebrospinal fluid and plasma. **258**, 245–258 (2000).
103. Schmidt, S. D., Nixon, R. A. & Mathews, P. M. ELISA method for measurement of

amyloid- β levels. *Methods in Molecular Biology* vol. 299 279–297 (2005).

Acknowledgments

Danila del Giudice acknowledges the EU funding within the Horizon 2020 Program, under the FET-OPEN Project “SensApp”, Grant Agreement n.829104.